

The mechanisms of sea ice melt pond formation and evolution

Chris Polashenski,¹ Donald Perovich,² and Zoe Courville²

Received 20 April 2011; revised 27 October 2011; accepted 6 November 2011; published 5 January 2012.

[1] A series of observations were made on melting first year, landfast Arctic sea ice near Barrow, Alaska to explore the seasonal evolution of melt pond coverage. Observations of pond coverage, albedo, and ice properties are combined with terrestrial lidar measurements of surface topography and meltwater balance to quantitatively identify the timing and role of mechanisms driving pond coverage. The formation of interposed fresh ice is found to eliminate meltwater percolation through early pond formation and allow widespread ponding well above sea level. Pond drainage to sea level occurs principally by horizontal meltwater transport over the ice surface to macroscopic flaws. Freeboard loss, caused by buoyancy decline as the ice thins, controls pond growth late in the melt season after percolation begins. The majority of the macroscopic flaws that drain melt ponds to sea level are observed to develop from brine drainage channels within the ice. A simple thermodynamic model of meltwater percolation illustrates that fresh meltwater inflow causes pores in the ice to either shrink and freeze shut or enlarge based on initial size and ice temperature. This threshold behavior of pore diameter controls both the blockage of smaller pores with interposed ice and the enlargement of larger brine drainage channels to allow meltwater drainage. The results identify links between the temporal evolution of pond coverage and ice temperature, salinity, and thickness, providing new opportunities to realistically parameterize ponds and summer ice albedo within sea ice models.

Citation: Polashenski, C., D. Perovich, and Z. Courville (2012), The mechanisms of sea ice melt pond formation and evolution, *J. Geophys. Res.*, 117, C01001, doi:10.1029/2011JC007231.

1. Introduction

[2] Shortly after the onset of sea ice melt in the Arctic, meltwater begins to collect on the ice surface in visible pools referred to as melt ponds. The pooling water alters the light scattering properties of the ice surface and dramatically lowers albedo wherever melt ponds form [Perovich *et al.*, 2002a; Grenfell and Perovich, 2004]. The lowered albedo, in turn, changes both the amount and the partitioning of solar energy in the ice-ocean system. Increased absorption of sunlight in the ice and the upper ocean accelerates ice melt [Perovich *et al.*, 2003], while greater sunlight availability beneath the ice may enhance primary productivity [Light *et al.*, 2008]. Ponded ice which is subsequently drained of meltwater rapidly reforms a surface scattering layer of loose, decaying ice crystals, and returns to a high albedo, similar to that of ice that never ponded [Perovich *et al.*, 2002a]. The spatial coverage of melt ponds is therefore a predominant control of albedo and solar energy partitioning on melting Arctic sea ice [Eicken *et al.*, 2004], and, because of the importance of albedo feedbacks in the Arctic, is a variable of considerable interest in climate modeling.

[3] Despite the importance and ubiquitous presence of ponds during melt, relatively few comprehensive observations of pond coverage have been collected in the Arctic. Efforts to collect such data are limited by the hazards of operation on melting ice, the difficulty differentiating ponds from open water in remote sensing [Fetterer and Untersteiner, 1998], and the persistent presence of low clouds during Arctic summer, which restrict aerial and satellite based observations [Perovich *et al.*, 2002b]. The lack of a long-term, intercomparable data set severely hampers any assessment of trends or potential feedbacks in the behavior of ponds, though it is generally conjectured that pond coverage in the Arctic is increasing due to increased presence of first year ice [Eicken *et al.*, 2004]. Available observations show that spatial coverage of melt ponds is highly variable and dynamic, particularly early in the melt season and especially on first year ice. Areal pond coverage on undeformed first year ice has been observed to range from 0% to 75% at a single site, with rates of change as high as 35% coverage per day [Scharien and Yackel, 2005]. A compilation of multiple study results tracking pond coverage, presented in Figure 1, illustrates that both absolute pond coverage and seasonal evolution of pond coverage exhibit large inter-annual and spatial variability [Barry, 1983; Derksen *et al.*, 1997; Hanesiak *et al.*, 2001; Nazintsev, 1964; Tschudi *et al.*, 2008].

[4] This variability presents significant challenges for realistic ice albedo simulation within sea ice and climate models. Semi-empirical ice albedo models, which set albedo based on seasonal transition points, rely on an assumption

¹Thayer School of Engineering, Dartmouth College, Hanover, New Hampshire, USA.

²Terrestrial and Cryospheric Sciences Branch, CRREL, Hanover, New Hampshire, USA.

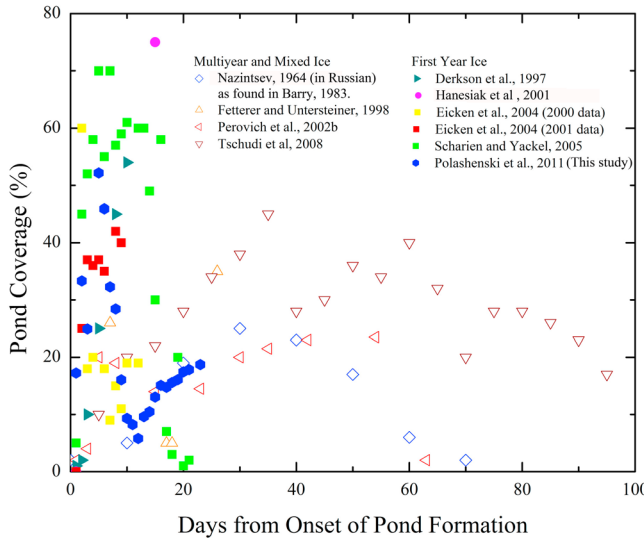


Figure 1. A compilation of published pond coverage data plotted on a time scale normalized to the start of pond formation. Solid markers denote FYI measurements while hollow markers denote multiyear or mixed ice measurements.

that the albedo between the transitions can be uniformly represented across ice types and locations. Such models represent changing seasonality well and can produce realistic annual energy fluxes when the selected summer ice albedo matches observations [Perovich *et al.*, 2002a]. Substantial spatial variability in observed ponding behavior, however, suggests that fixed empirical representations of summer ice albedo likely lack generality for other ice types and locations. Temporal variability of melt pond coverage also creates substantial intra-annual discrepancies between modeled and observed albedo [Perovich *et al.*, 2002a]. Linkages between pond coverage, albedo, and melt rates, which have the potential to result in significant pond-related albedo feedbacks, make even these short-term deviations important. Ensuring realistic prediction of albedo will require incorporating the mechanisms that drive pond coverage into models. A substantial effort is already being undertaken to do this by improving both small and medium scale models of melt pond coverage [Skillingstad *et al.*, 2009; Flocco and Feltham, 2007; Lüthje *et al.*, 2006; Taylor and Feltham, 2004] and incorporating explicit melt pond parameterizations into albedo calculations of global climate models [Flocco *et al.*, 2010; Hunke and Lipscomb, 2010; Pedersen *et al.*, 2009]. In the absence of basin wide pond observations and long-term data sets, supporting these efforts to create computationally efficient, yet physically representative models, requires further advances in our understanding of the mechanisms which drive the seasonal evolution of pond coverage.

[5] The principal goal of this work is, therefore, to improve understanding of the processes guiding the seasonal evolution of melt ponds on Arctic sea ice. The paper begins with a background section describing the discrete stages of seasonal pond evolution, which have been linked to meltwater balance and ice topography. Further background is presented on the percolation of meltwater through sea ice, highlighting several hypotheses for explaining the apparent

contradiction that melt ponds form well above sea level, upon ice which is expected to be quite permeable. A methods section then describes field observations and data processing techniques used to quantify the evolution of pond coverage, as well as the roles of meltwater balance, topography, and physical ice processes in driving the pond coverage evolution. The results of these observations are then presented, beginning with observations of pond coverage in which we identify the stages of pond evolution. This is followed by a quantitative analysis of the roles ice topography and specific terms of the meltwater balance play in driving these stages. Further analysis clarifies how ice-meltwater interactions control the availability of meltwater outflow pathways, enlarging brine drainage channels to create macroscopic flaws while plugging smaller porosity with interposed ice to prevent early season meltwater percolation. A model of meltwater flowing into a brine channel is presented which supports this hypothesis, showing that initial channel diameter controls whether meltwater entering into a pore refreezes, blocking the pore, or enlarges the pore by melting its walls. Finally, we include a discussion of the albedo and surface energy impacts of melt ponds, and compare our pond observations to predictions based on GCM pond parameterizations, forced with data measured at our field site, before concluding.

2. Background

2.1. The Stages of Pond Evolution

[6] Many factors are known to influence the development of melt ponds. When thought of as a hydraulic feature, a melt pond can be represented as a volume of water determined by the balance of inflows and outflows, distributed in the lowest points of local topography. This meltwater accounting conceptualization, schematically shown in Figure 2, is reflected in the general approach of some GCM pond parameterizations [e.g., Hunke and Lipscomb, 2010; Pedersen *et al.*, 2009]. Inflow rates to ponds are determined by melt rate, precipitation, and the size of a pond's catchment basin. Outflow rates depend on both hydraulic head and the presence of outflow pathways. Outflow can proceed either by vertical percolation through connected pore structures in the ice or by horizontal movement of water across the surface of the ice to macroscopic flaws, such as cracks, leads, seal breathing holes, and as we describe later, enlarged brine channels. Topographic relief depends on myriad factors, including deformation history, snow drifts, ice freeboard, and past seasons' melt, but is generally known to be lower on undeformed FYI than on undeformed multiyear ice (MYI).

[7] Past observations have demonstrated that the evolution of seasonal pond coverage is characterized by four general stages, defined by descriptions of pond behavior and control mechanisms [Eicken *et al.*, 2002]. The first stage begins with the onset of pond formation and is characterized by a rapid rise in pond coverage as meltwater accumulates on the surface of relatively impermeable ice. Pond volume is controlled by melt rate and the loss of meltwater through lateral transport to cracks and flaws. Outflow pathways are limited and ponds typically form well above sea level. Topographic relief of the ice, which governs how meltwater is distributed on the ice surface, is predominantly

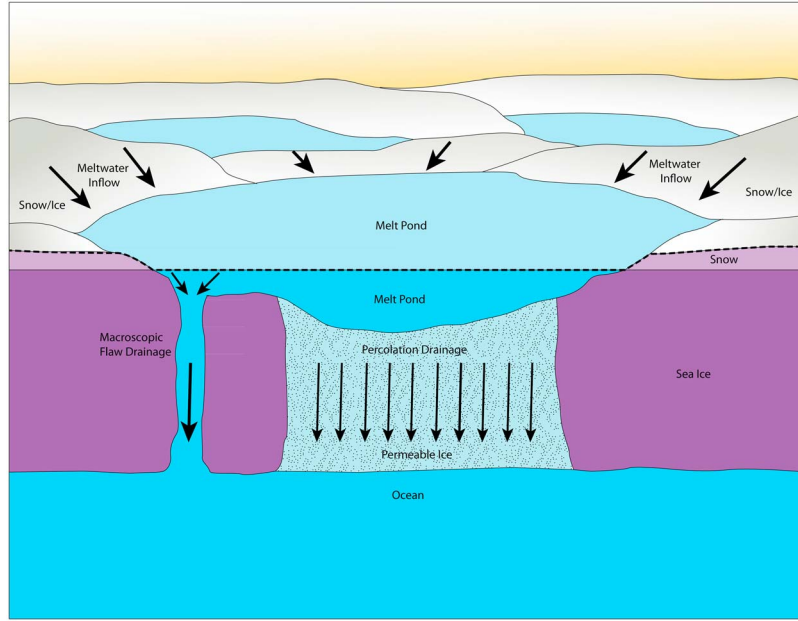


Figure 2. Idealized illustration of a melt pond, showing meltwater flux pathways.

dictated by forces that occurred prior to the onset of melt such as deformation, snow drifting, and, on MYI, hummock creation during previous melt seasons. Due to the topographic relief created by hummocks, ponds on MYI tend to be confined to deeper pools with less spatial coverage than on FYI where limited relief results in shallow, but widespread, ponding. Pond coverage on undeformed FYI frequently spikes to 50% or more during this period, while coverage on multiyear ice exhibits a more subdued peak. Because this first stage results in very low albedo and coincides with near peak solar input in much of the Arctic, its duration can be quite important to seasonal energy balance.

[8] During the second stage, the majority of the ponds drop from well above sea level to very near sea level (<0.02 m deviation) due to increased outflow. Pond coverage drops substantially on FYI, but only slightly on multiyear ice. Both percolation through the ice [Eicken et al., 2002] and continued horizontal transport to macroscopic flaws [Scharien and Yackel, 2005] are cited as significant causes of water loss during this time, though our data show that horizontal transport dominates.

[9] During the third stage, ponds remain very near sea level because outflow pathways are no longer limiting. High ice permeability and open macroscopic flaws mean that water can be freely lost to the ocean if very slight (<0.005 m) hydraulic head develops. Many ponds melt through to the ocean during this stage, and the ice may decay entirely. Though meltwater is no longer accumulated above sea level, pond coverage on both ice types increases steadily, often to its seasonal maximum. Increases in pond area during this time instead occur by creating new areas where the local surface height is below freeboard. These areas may be created either by lateral melt at the walls of the ponds or by a change in overall ice freeboard as the ice thins and buoyancy force is lost. Given these mechanisms of pond growth, changes in topographic relief now play a larger role in determining pond coverage.

[10] The fourth stage, refreezing, is not restricted to the end of the season. At any time during this seasonal evolution, changing atmospheric forcing may result in freezing conditions, which can stop meltwater inflow and cause a skim of ice to form over many ponds. A thick dusting of snow on top of this ice can temporarily erase the albedo effects of the ponds [Grenfell and Perovich, 2004].

2.2. Ice Permeability

[11] The descriptions of processes occurring within each of the first three stages of seasonal pond evolution indicate that changes in the availability of meltwater outflow pathways are expected to trigger the variations in pond coverage observed. These outflow pathways can be grouped into two types; connective porosity in the ice through which meltwater can percolate and macroscopic flaws to which meltwater is transported by horizontal flow over the ice surface. A range of macroscopic flaws, including seal breathing holes [Holt and Digby, 1985], cracks [Eicken et al., 2002], and the edge of floes [Fetterer and Untersteiner, 1998], have been noted to drain substantial amounts of meltwater, particularly early in the melt season. Percolation through porosity in the ice has been observed by tracer and bail hole experiments, and is expected to occur at widely varying rates throughout the melt season [Eicken et al., 2002]. The relative importance of the two outflow pathways to the meltwater budget is, at best, only qualitatively known.

[12] An increase in brine volume, and therefore porosity, in warming ice is expected to bring about percolation as the ice pore structure becomes connective. The resulting permeability transition, occurring as ice temperature rises, has been cited as a meltwater balance control mechanism potentially controlling pond drainage during parts of the melt season [Golden, 2001; Eicken et al., 2002]. This permeability transition has been explored theoretically by the application of percolation theory [Golden et al., 1998] and continuum models [Petrich et al., 2006] and experimentally

through observations of Antarctic ice flooding [Golden, 2001], the use of X-ray computed tomography [Pringle et al., 2009; Golden et al., 2007], and field tests with a bail hole technique similar to that used in terrestrial hydrology [Freitag and Eicken, 2003; Eicken et al., 2004; Kawamura et al., 2006]. Percolation theory predicts that the connectivity of brine-filled pores will increase very rapidly when porosity nears a critical fraction. Adapting theory used in the study of compressed powders to the specific geometry of sea ice has produced predictions of this threshold at 5% brine volume [Golden et al., 1998], consistent with observations [Ono and Kasai, 1985]. Using well known relationships between temperature, salinity, and brine volume [Frankenstein and Garner, 1967], however, it can be shown that a brine volume of 5% is reached in typical FYI well before melt ponds begin to form; suggesting that the bulk of the ice beneath the ponds is substantially permeable. Measurements of the Darcian permeability constant beneath ponds on summer ice of between 10^{-9} and 10^{-11} m^2 support this [Freitag and Eicken, 2003]. Early summer observations of widespread pond formation above sea level, however, require that the ice remain relatively impermeable to downward percolation, with permeability constant substantially less than 10^{-12} m^2 [Freitag and Eicken, 2003], well after the brine volume has passed 5%.

[13] The discrepancy is believed to lie in the uppermost layers of ice [Eicken et al., 2002], in which direct measures of permeability, such as the bail hole tests, are not possible, and where several assumptions of the percolation model may not hold. This portion of FYI, which is typically of granular structure, is expected to have lower pore connectivity than the columnar ice below, resulting in a higher porosity threshold for percolation and lower permeability in general [Golden, 2001]. Also, a layer of superimposed fresh ice with lower expected porosity that forms when snowmelt refreezes on the ice surface may effectively seal the ice surface. Though most references identify superimposed ice as a discrete layer composed entirely of refrozen snowmelt that forms on top of the existing sea ice [e.g., Granskog et al., 2006], at least one describes superimposed ice extending into the uppermost part of the sea ice [Freitag and Eicken, 2003]. Under the latter definition, superimposed ice may consist of a mixture of sea ice and refrozen meltwater formed when snowmelt percolates into the pores of the sea ice and refreezes. We observed both phenomena and note that the two appear to play different roles, sufficiently unique to merit clear separation. We therefore refer to the second mechanism, in which the “superimposed ice” is formed within the matrix of the sea ice, as the formation of *interposed ice* in this paper.

3. Methods

3.1. Observations

[14] Field studies of melt ponds were conducted on seasonal, landfast Arctic sea ice in northern Alaska during the summer melt seasons of 2008, 2009, and 2010, with particular focus in 2009. Study periods ran each year from late May, prior to the onset of ponding, through mid to late June, when the ice became unsafe to work on. During this time, all of the snow and between a third and one half of the ice volume melted. Our key variables, pond coverage and

albedo, were measured along transect lines daily for the duration of the experiments during all three years. Meanwhile, a wide range of other measurements, targeting meltwater balance, ice topography, ablation, and surface properties, were taken in 2009 and 2010 to monitor phenomena identified as potentially important factors driving melt pond development.

[15] Measurements were collected at repeatedly visited sites just north of Barrow, AK, approximately 1 km offshore from Niksiuraq on landfast ice in the Chukchi sea, near 71.366 N, 156.542 W. The exact location of the observation sites was selected each year to represent level, snow covered first year ice. Close inspection showed that the area within sites ranged from pieces of absolutely flat, undeformed ice, to ice which had finger-rafter early in the growth season, to a very lightly rubbed field of 5–10 cm thick blocks. Though not strictly “undeformed,” the general character of the sites is considered typical of level first year pack ice in the adjacent Chukchi Sea [Shapiro and Barnes, 1991] and is the same ice type that is frequently referred to as undeformed in the literature. One measurement site was monitored in 2008 and 2010 while two sites, about 1 km apart were monitored in 2009. The 2009 sites represented slightly different ice types, with the north site including some lightly rubbed ice while the South site was very flat. The north site was also, fortuitously, located in a relatively small hydraulic basin which enabled us to better constrain meltwater balance there. Though the arrangement of the sites varied, Figure 3 shows a schematic of a composite site illustrating key features of the experimental setup. An area approximately 100 m × 200 m in size was marked off for non-invasive observation; principally by scanning with a terrestrial lidar scanner (TLS). These areas were left undisturbed throughout the campaign to the highest degree possible, ensuring natural pond progression. No one entered them during measurements, except for two times in 2009 when a single person walked in very carefully, traveling in melt ponds so as not to disturb the surface scattering layer, to measure meltwater flow at macroscopic holes located in the scan field. These measurements are discussed more in section 3.2. Along one 200 m edge of the non-invasive observation area a transect line was set up for measurements which required human presence. Surrounding the non-invasive observation area are platforms, stakes, and reflectors anchored into the ice for use during TLS data collection and registration. The size of the observation sites was selected to be 4–5 times the characteristic length of the snow drifts and melt ponds to collect a representative sample of the surface conditions.

[16] The 200 m transect, marked at the top of Figure 3, was set up with one side designated for travel, and the opposite left pristine for measurements. Travel along the transect was limited to the four foot-travel passes per day required to gather the measurements, and had no apparent effect on the surface evolution of the pristine side. A typical suite of daily measurements taken along the transect line included wavelength integrated albedos from 300 to 3000 nm measured every 2.5 m with a Kipp and Zonen albedometer, spectral albedos from 350 to 2500 nm taken every 5 m with an Analytical Spectral Devices FS3, and snow or pond depths taken every 0.5 m with a Snow-Hydro automatic snow depth probe. Albedo measurements were collected by mounting the sensor on a 1.5 m long arm and positioning it

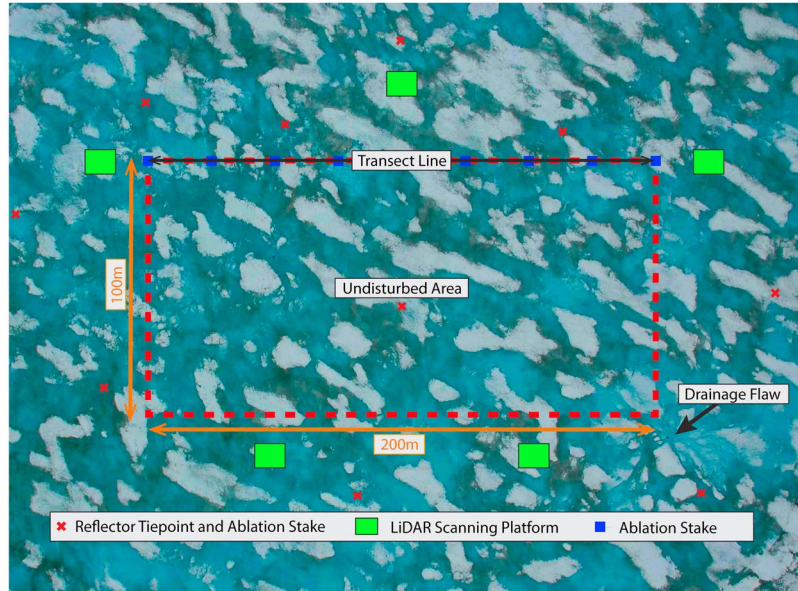


Figure 3. A composite schematic showing features of a typical observation site overlaid on an aerial photo taken near the north site from approximately 300 m altitude.

~1 m above the snow surface to minimize shadowing [Grenfell and Perovich, 2004]. The surface conditions along the line were photographed every 2.5 m and the surface type was characterized to 0.1 m resolution using a tape measure laid along the transect. Also along the transects, ice thickness was measured prior to the onset of melt using an EM-31 electromagnetic induction sensor [Eicken et al., 2001] and at the end of the experiment using a thickness tape in holes drilled every meter along the line. Snow density cores were taken just away from the line to represent the range of snowpack depths present without disturbing other measurements. Depths were recorded and cores were weighed in the lab for density calculation.

[17] Non-invasive study areas were present in 2009 and 2010. In 2009, these areas were repeatedly photographed from a kite- or airplane-borne camera as the melt season progressed, whenever cloud conditions permitted. Kite-borne images were captured with a Canon Powershot SD 890 triggered by an FM remote control servo, suspended below the kite line by a 4 point harness. Airplane based images were captured with a Nikon D70 SLR camera mounted in a custom cradle and triggered to take images with a remote intervalometer. Image mosaics were constructed using PTGui and Autopano Pro software.

[18] In both 2009 and 2010, the non-invasive study areas were scanned with a TLS approximately every other day, as wind, fog, and precipitation permitted, to generate detailed maps of the surface topography. The scan data was captured with a Riegl LMZ-420i scanning unit using a 1500 nm laser mounted on a tripod ~2.5 m above the ice surface. The tripod was erected on specially built platforms, which were frozen into the ice in early April. This eliminated scanner movement relative to the melting ice during scans; a significant problem in earlier attempts. The scans captured from each platform were registered to one another using 10 fixed cylindrical retro-reflectors as registration points to create a full point cloud of the site surface using Riscan Pro software.

The standard deviation of tie points calculated during registration of scans from a given day is typically less than 5 mm, but as high as 10 mm on particularly windy days (>10 m/s) when stabilizing the scanner became difficult. Artifacts caused by laser reflection from melt pond surfaces, fog, or precipitation, are removed in Quick Terrain Modeler and Matlab software. Surface measurement density is highly dependent on proximity to the scanner and slope aspect of the surface and the lowest point densities are about 150 points/m², near the center of the study area. Melt ponds generally do not reflect the near infrared laser used by the scanner strongly enough to register a direct return. Tying the ring of lowest return points collected at the rim of the pond, however, allows satisfactory representation of the pond surface level when a digital elevation model (DEM) is created from the point cloud.

[19] Translational ice movement prevented the use of DGPS reflector locations for co-registration of point clouds taken on different days. Instead, we left the reflectors frozen in place for the duration of the experiment and registered all scans to the reflector array as if it were static. The use of this ice-based reference assumed there was very minimal deformation in the ice within the reflector array. Standard deviation of registration between daily reflector position arrays and the “true” position array does not exceed 1.5 cm, indicating that this was a reasonable assumption. The slight deformation which did occur was found to accumulate gradually and deviation between consecutive day’s reflector arrays (<7 mm) was near the accuracy of the scanner. Deformation in the reflector array did result in a slight tilting of the registered scans with respect to the X-Y plane over the study duration, by as much as 2.5 cm vertical per 100 m horizontal. To avoid the unrealistic result of slightly tilted water surfaces, we chose to correct the projection of the data onto the coordinate system using the inclinometer data collected by the scanner at the expense of a slight loss in absolute accuracy.

[20] Surface elevations collected by the scanner compare very well with manual laser survey profiles and fixed ablation stake readings. Average bias compared to these methods is below 1 cm and standard deviation of individual points is 2–3 cm, due mostly to scatter in individual scan returns and differences in the exact sample locations between methods. With all errors and corrections in consideration, the comparison of consecutive day's average surface height measurements at the centimeter level remains reasonable. Total surface height location error compounded over the melt season is less than 5 cm, which, given total ablation of about 50 cm, translates to under 10% error.

[21] As part of our efforts to monitor the movement of meltwater into and through the ice, 10 cm diameter ice cores were taken every 2–3 days from which temperature, salinity, and stable isotope ratios were measured. Holes created during coring have been observed to drain substantial amounts of meltwater, significantly altering the area melt ponds. Because of this, the ice coring site was selected each year more than a kilometer away from the primary observation site in ice of the same character. Cores used for salinity and isotope measurements were cut into 5 cm sections and bagged immediately after extraction to minimize brine drainage. Temperatures were measured out of direct sunlight at the center of a second adjacent core by inserting a temperature probe into holes drilled into the core within a few minutes of extraction. Samples collected for salinity and isotope measurement were melted in double sealed bags at room temperature. A sample from the well mixed bag was taken in a glass vial for later isotope analysis, then salinity measurements were made with a YSI 30 conductivity probe having stated measurement error of 1% of bulk salinity. Isotope samples were sent to the University of Utah Stable Isotope Ratio Facility for Environmental Research for measurement on a PICARRO Wavelength Scanned Cavity Ring-Down Spectrometer. Standard uncertainty determined from laboratory standard samples is 1.6 $\delta^{2\text{H}}$ and 0.1 $\delta^{18\text{O}}$.

[22] Apart from the repeated measurements at the study sites, a number of other measurements were made or are available from nearby projects, including bottom melt rates and temperature profiles in the ice from the Barrow Ice Observatory mass balance site located adjacent to our site and radiation measurements from the DOE ARM site 4 km away.

3.2. Calculating Meltwater Balance

[23] Lidar surface height data, reported in reference to an X-Y plane defined within the ice, provided a means to track the loss of meltwater from the ice surface. The surface height of a location represents the sum of the thicknesses of ice, snow, and liquid water present above the reference plane; $h_{\text{total}} = h_{\text{ice}} + h_{\text{snow}} + h_{\text{water}}$. Using the average thicknesses and density of each phase, we calculate the total mass of water in snow, ice, and liquid forms above the reference plane according to equation (1)

$$m_{\text{water}} = A_p (\rho_{\text{ice}} \bar{h}_{\text{pondedice}} + \rho_{\text{water}} \bar{h}_{\text{water}}) + (1 - A_p) \cdot (\bar{\rho}_{\text{snow}} \bar{h}_{\text{snow}} + \rho_{\text{ice}} \bar{h}_{\text{bareice}}), \quad (1)$$

where $\rho_{\text{ice}} = 900 \text{ kg/m}^3$, $\rho_{\text{water}} = 1000 \text{ kg/m}^3$, and $\bar{\rho}_{\text{snow}}$ is the average snow density measured on or nearest the scan date (typically varying from ~ 250 to 500 kg/m^3), A_p is the

pond coverage fraction (which varied from 0 to 0.75), and \bar{h}_{snow} and \bar{h}_{water} are the average snow thickness ($<0.35 \text{ m}$) and average pond depth ($<0.3 \text{ m}$). Repeatedly entering the lidar field to measure snow and water depth would disturb pond evolution, so average snow and meltwater depth are estimated based on 400 daily measurements taken along the adjacent transect line. Average ice thickness above the reference plane is calculated separately for ponded and unponded surfaces as the difference between the average surface height and the average snow or water depths so that $\bar{h}_{\text{pondedice}} = \bar{h}_{\text{pondsurface}} - \bar{h}_{\text{water}}$ and $\bar{h}_{\text{bareice}} = \bar{h}_{\text{baresurface}} - \bar{h}_{\text{snow}}$. Pond locations are determined directly from the lidar scans, as ponded areas produce no return. The generality of using the snow and pond depth measurements from the transect to represent the scan area was tested twice by measuring 5000+ depths in the area adjacent to the transect. Both times, average depths from the larger sample were consistent with those found along the transect within 1.5 cm. The “snow” in measurements of \bar{h}_{snow} and $\bar{\rho}_{\text{snow}}$ included the surface scattering layer of deteriorating ice crystals after actual snow melted away.

[24] The total amount of meltwater lost from the ice surface is calculated by subtracting the mass of water above the reference plane on the date of interest from the amount present at the start of the melt season

$$\Delta m_{\text{water}} = m_{\text{water}}(0) - m_{\text{water}}(t). \quad (2)$$

[25] During the 2009 experiment, a special effort was made to directly measure meltwater flow down macroscopic flaws, such as cracks and seal holes, at the same time as the TLS observations were being collected for comparison to TLS derived water mass loss. The meltwater flow rate down each flaw was calculated by measuring the profile and flow velocity of channels which fed the draining hole. Depth was profiled every 10 cm across the channels and flow velocities were calculated by placing a floating object in the water and timing its movement along a measured path with a stopwatch. The velocity was measured several times, midstream as well as closer to the edges and averaged. Flow, Q , was then calculated as in (3)

$$Q = 0.9vA, \quad (3)$$

where A is the cross-sectional area of the stream, v is the flow velocity averaged over several measurements, and 0.9 is a simple correction factor relating average velocity to surface velocity for flow over a smooth streambed [Rantz et al., 2005].

[26] Both the total flow rate into the holes, and the total water drainage calculated from the lidar are converted to units of water depth (equivalent to volume per area, m^3/m^2) for inter-comparison by dividing the volumetric flow rate Q by the area measured

$$\Delta h_{\text{water}} = \frac{Q}{A_{\text{measurement}}}. \quad (4)$$

[27] The 2009 north site, situated on a pan of ice surrounded by a low ridge, presented an opportunity to measure outflow within a closed basin. The drainage basin, shown in

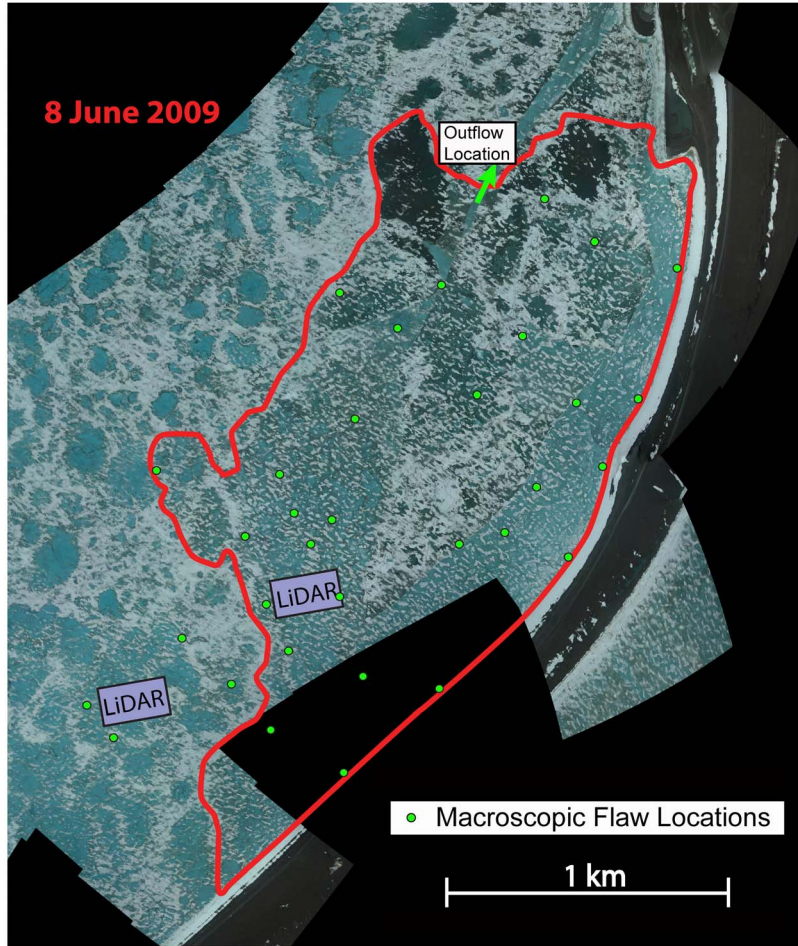


Figure 4. Aerial view of the 2009 north site drainage basin taken 8 June with drainage flaws on 10 June marked.

an aerial view in Figure 4, was roughly 1.3×1.7 km in size, or 2.29 km^2 in area via GPS outline. Because of the basin size and the large number of holes, total flow rate could not be measured directly at all of the holes every day. Instead, total flow was calculated by systematically locating and measuring the flow down all holes in the drainage basin at two points in the melt season, when aerial photos were available to aid the efforts, then extrapolating the flow on other days. Data needed to extrapolate from the baseline flow were gathered by repeated measurements of flow rate at a subsample of the holes, and monitoring a subset of the basin area for development of new holes.

[28] Twenty-nine holes were cataloged in a basin wide survey on 8 June (shown on Figure 4), while forty-six holes were cataloged in another basin-wide survey on 10 June. Total water drainage rate from the basin on these days was calculated at $1.56 \text{ m}^3/\text{s}$ and $0.73 \text{ m}^3/\text{s}$ respectively; the equivalent to 5.9 cm and 2.8 cm of water loss per day, distributed over the entire surface. As the melt season progressed, the density of holes in the sub sampled $400 \text{ m} \times 600 \text{ m}$ area increased, while the flow rate down each of the monitored holes decreased. Total flow was calculated by assuming that the flow rate at all of the holes that existed during the baseline surveys followed the trends observed at the sustained monitoring holes, and that new holes appeared

over the entire basin after the baseline surveys with the same density and flow rate as in the sub-sampled area.

[29] The error in this set of extrapolations is difficult to quantify, but constrained by several known points. First, there was no flow downholes prior to 7 June 2009 because ground and aerial observations showed that holes did not yet exist. Second, flow was directly measured at all of the holes on 8 June 2009 and 10 June 2009. Third, by 15 June 2009 flow was near zero again because flow down all of the holes had ceased to be measurable. These data points are sufficient to establish the conclusions of the following sections. The extrapolations should be viewed as a best estimate for the intervening times.

4. Results

4.1. Pond Evolution

[30] Pond coverage varied tremendously during the course of each field campaign. In contrast to the observations compiled in Figure 1 from different locations and ice types, however, pond coverage followed a similar seasonal evolution each year. A plot of pond coverage versus date, monitored along our transect lines during each of the three years can be found in Figure 5a. Shifting the time scale to remove variation in the onset date of pond formation (Figure 5b)

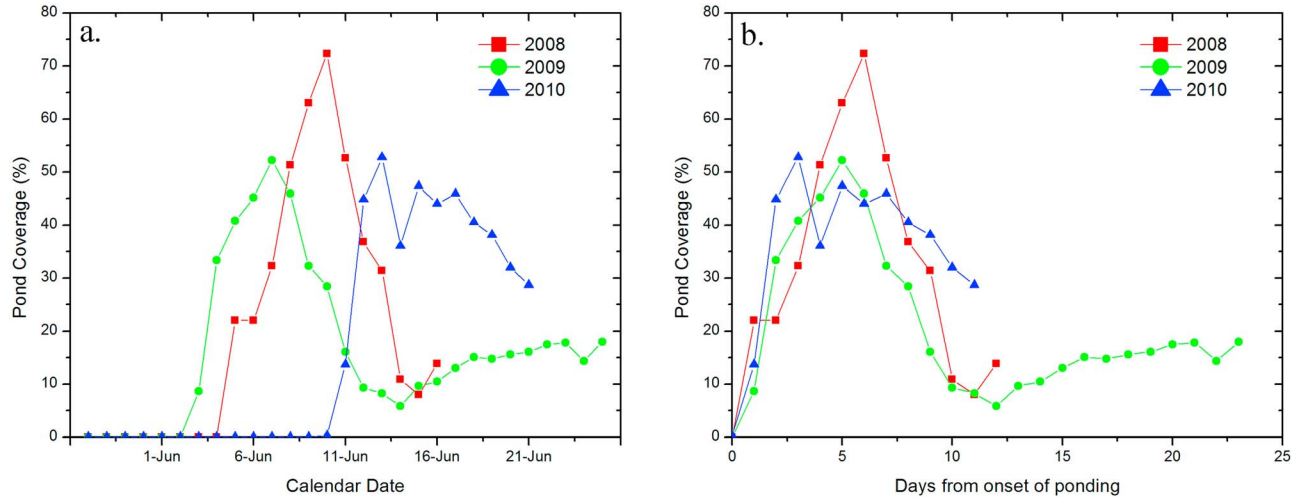


Figure 5. (a) Melt pond coverage versus calendar date and (b) melt pond coverage versus days since onset of pond formation.

highlights the similarities in the pattern of pond evolution from year to year. On this plot we can identify the first three general stages of pond coverage development described above. Once pond formation began, coverage rapidly increased for 4–6 days to a peak at more than 50% (stage I), then coverage declined for the next 5–7 days to a minimum (stage II). After this, coverage gradually increased for the remainder of our time on the ice (stage III). The dramatic change in the icescape caused by the rapid dynamics of pond evolution is captured by a series of dated composite aerial photos and lidar scans presented in Figure 6.

4.2. Mechanisms of Pond Evolution

[31] As discussed in the background section, meltwater balance and surface topography both exert control over pond evolution. The observations collected in this study provide a means to more specifically quantify the role of these two general mechanisms in driving the observed pond evolution.

4.2.1. Topographic Control of Pond Coverage

[32] The lidar surface elevation measurements enabled us to observe ice topography in great detail prior to melt and as it evolved through the melt season. Premelt ice topography was expected to play a key role in determining the location and peak coverage of melt ponds by controlling the distribution of meltwater. Most of the surface relief at the sites, however, was created by snow atop the ice, rather than the ice itself. The importance of the combined snow and ice relief was investigated by comparing pond locations throughout the melt season with the premelt snow topography at those locations. Each day that lidar scans were taken, the vertices of a 10 cm grid over the study site were denoted as either ponded or unponded. The scanner's 1500 nm laser generally produces no return from liquid water so the surface state within each cell was determined based on whether a return was received from within the cell (unponded) or not (ponded). The average premelt surface height in each ponded grid cell was then retrieved from scan data taken a week prior to pond formation. The surface height distribution of ponded areas is divided by the total premelt height distribution to calculate the fraction of premelt surface of a given height that is ponded on the date of interest. These

distributions are plotted in Figure 7a. The high fraction of areas with low premelt surface height pond covered during stage I (6 and 7 June) confirms that premelt surface height, dictated largely by snow dune formation, is a strong control of whether ponds will form at a given location. The use of individual lidar returns and slight surface height differences between unconnected ponds across the site induce 2–3 cm of scatter in the apparent fill line, but by peak pond coverage on 7 June, 95% of the points which had a premelt surface height of less than 0.35 m are pond covered, while only 17% of those which had a height over 0.39 m are ponded. Furthermore, the percentage of the cumulative premelt surface height distribution (dashed black line) that was below the fill level (54% below 0.38 m), is in close agreement with the pond coverage of 52% on 7 Jun. The effect of premelt topography during stage I is further evident visually in Figure 8, which shows a height-colored image of the premelt season surface, and an adjacent height-colored image of just those areas which were pond covered on 7 June.

[33] As the pond coverage drops during stage II (8–13 June 2009), the orderly filling of points with the lowest premelt surface height is not strictly preserved. Pond coverage in areas where premelt surface height was just below the fill line drops first; but not to zero. The very lowest premelt areas continue to have the highest pond coverage, but not nearly 100%. Figure 7a shows that by 13 June, when pond coverage reaches its minimum, most of the premelt height categories below the fill line still have about 5% of their area pond covered. Cumulative distributions of the premelt surface height in ponded areas, presented in Figure 7b, show that the distribution of premelt surface heights in ponded areas does not change much as ponds drain. Essentially, the areas which remain pond covered for the rest of the melt season are a subset of those areas which were ponded at peak coverage, but there is not a strict preference for the areas of lowest initial surface height. That all points of initial height below the fill-level appear to have similar likelihood of remaining ponded regardless of premelt height suggests that another control of topography, which operates only in the ponded covered areas and without respect to initial surface height, enhances relief during stage II. Two such controls

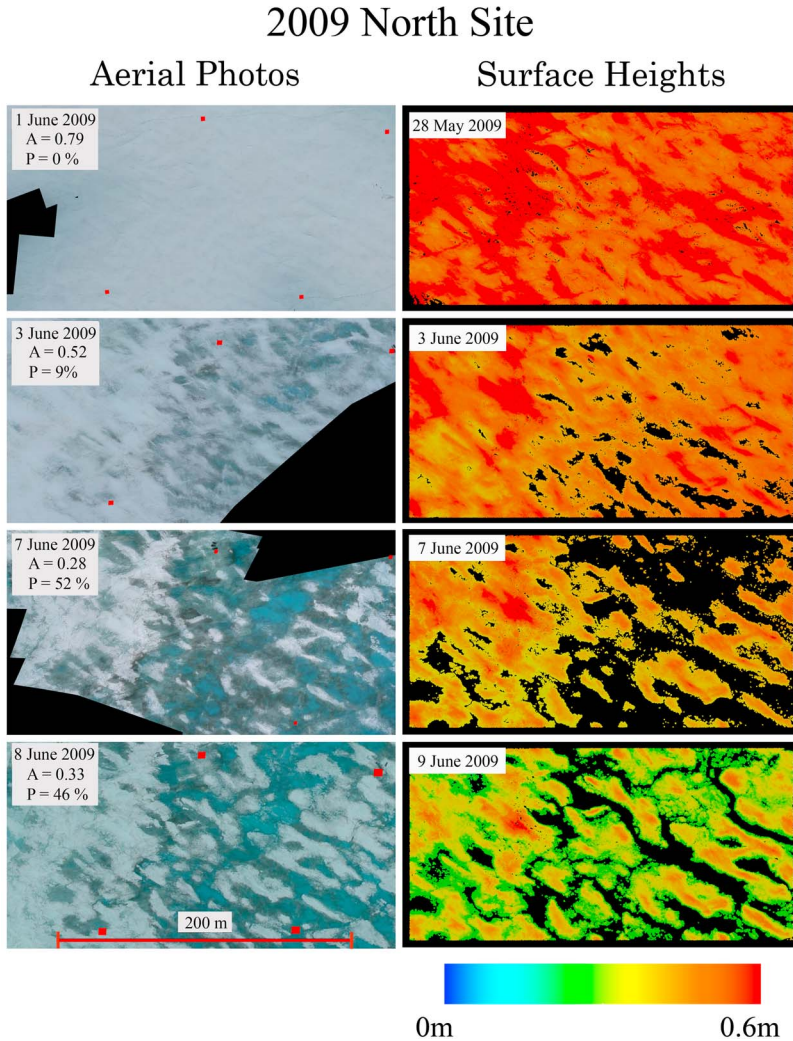


Figure 6. Composite of kite and plane based aerial photos and height colored surface maps created from TLS during melt season at the 2009 north site. There is a scale on the lower left aerial photo while the TLS images are 100 m × 200 m in size. All images are dated in the upper left corner. Albedo (A) and pond coverage (P) are presented on the aerial photos.

appear significant during stage II; the presence of sediment in the ice, and flow toward drainage points in meltwater channels. Both enhanced ablation in pond bottoms and appeared to be spatially uncorrelated to initial surface height. Qualitative observations suggest that both processes can locally enhance pond bottom ablation rates by 50–100%, and that the pond locations on 13 June were strongly correlated to these processes. Determining the importance of these factors in creating the below sea level pond depressions that remain ponds after stage II will require further study.

[34] During stage III, abundant outflow paths maintain pond surfaces near sea level. Increases in pond area occur only when the surface height of new areas drops below sea level. Two potential mechanisms were identified that increased the area where the ice surface is below sea level; lateral melt at the walls of the ponds and losses in overall ice freeboard occurring as ice thinned and buoyancy force declined. The locations where ponds grew during stage III at the 2009 N site, highlighted in blue in Figure 9a, suggest that

freeboard decline caused most of the pond growth in stage III. The horizontal rate of growth at some pond edges, working out to as much as 1 m per day, is much higher than lateral heat transfer would be expected to cause. Also, the pattern of growth shows no preference for pond walls that faced into the prevailing wind, where waves would be expected to enhance lateral heat transfer. Growth did appear, however, to be concentrated in areas where surface height was low at the start of stage III (compare Figure 9a, showing where ponds grew, to Figure 9b showing areas within 7 cm of sea level on 13 June). Cumulative distributions of all surface heights at the start of stage III and of just the areas where ponds grew during stage III can be seen in Figure 10. Approximately 85% of the area where ponds grew was within 7 cm of sea level at the start of stage III compared to only 20% of all unpended surfaces at that time.

[35] During the same part of stage III, the lidar data show that the average ice freeboard declined about 4 cm; roughly what is expected from buoyancy loss due to the ~35 cm ice thinning observed during this period. Even allowing for

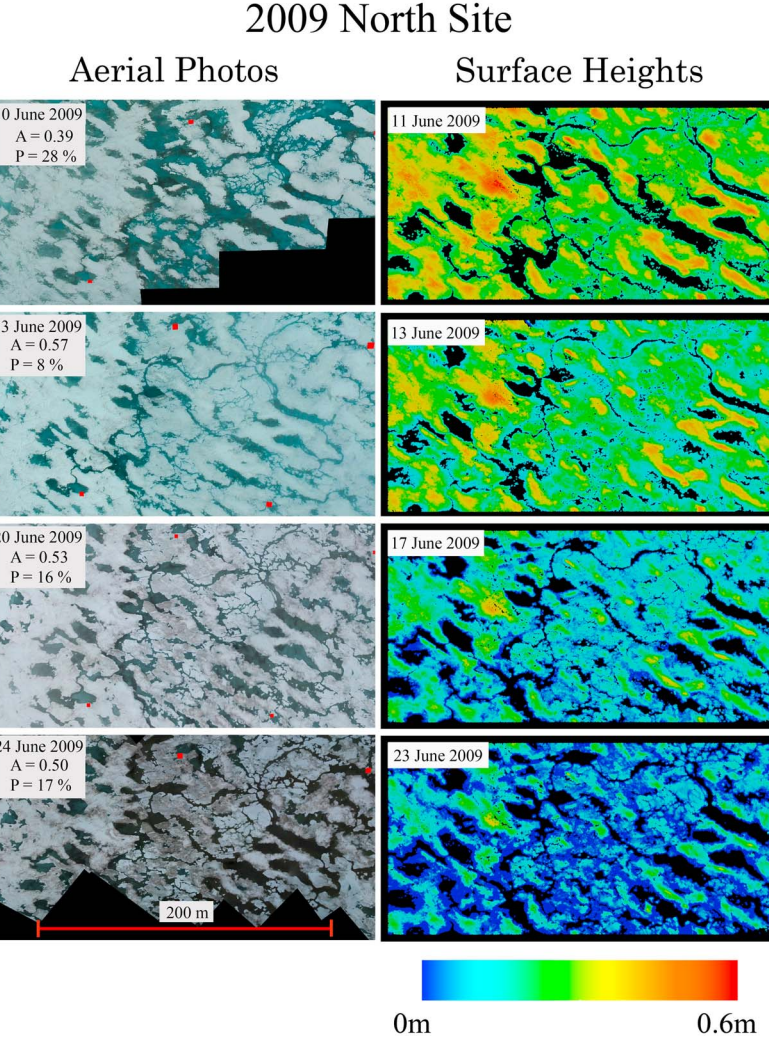


Figure 6. (continued)

2 cm of scatter in individual lidar measurements widening the height distribution, some areas which ponded were slightly higher than would have been flooded if topography was simply preserved. Still, ponds formed almost entirely on the areas closest to sea level. Combined with the observation that areas of ice with very low freeboard become darker and melt at higher rates as their surface scattering layer thins, it seems reasonable to conclude that the freeboard decline controlled pond growth and resulted in flooding areas 2–3 cm higher than would have been flooded if topography was simply preserved.

[36] While freeboard loss appears to dominate pond growth during the first 10 days of stage III, roughly half of the starting ice mass remained when we left the ice. In order for ice freeboard to continue to be the predominant mechanism of pond growth during later melt, large areas of ice near freeboard must remain that will flood with incremental losses of freeboard. Because of preferential melt in the ponds, however, we would expect ponds to sink into ever deeper wells where the effects of freeboard loss would be damped. Lateral melt might then take over as the predominant growth mechanism. To examine the extent to which this occurred

during the first part of the melt season, we plot cumulative distributions of the surface height for scans taken during stage III, in relation to sea level at the time of each scan (Figure 11). The amount of ice within 5 cm of freeboard changes very little during our observations and still covers 10% of the total area on 23 June, suggesting that freeboard loss continued to control pond growth after our departure.

4.2.2. Water Balance Control of Pond Coverage

[37] While topography controlled pond location and meltwater distribution, qualitative observations collected during our study suggested that changes in the availability of meltwater outflow pathways dictate the timing of stages in seasonal pond evolution. During the rapid rise in pond coverage of stage I, pond surfaces were well above sea level, indicating that outflow pathways were very limited. The first noted appearance of macroscopic holes draining meltwater from the surface each year coincided with the first day of pond coverage decline in stage II. Combined with evidence of rapidly dropping pond levels, the appearance of the holes appeared to significantly enhance outflow. Flow slowed at the macroscopic holes as pond level approached sea level, ceasing entirely as the ponds reached a minimum coverage

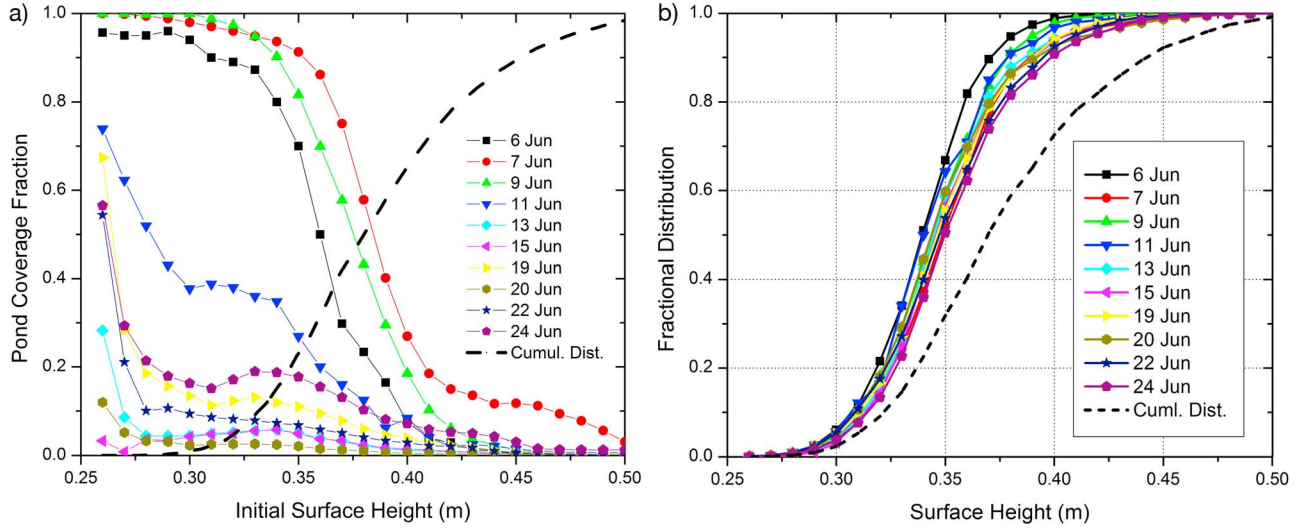


Figure 7. (a) Distributions showing fraction of premelt surfaces of a given height that are ponded on date identified in the legend and (b) cumulative distribution of premelt surface height at pond covered locations by date, both at 2009 south site.

at the end of stage II. Thereafter, no meltwater flow could be detected at the macroscopic holes, though ablation continued at several centimeters per day. Pond levels remained fixed to very near sea level and significant mass loss continued, indicating that meltwater was now leaving the surface by another means; presumably percolation through the ice.

[38] Calculations of meltwater loss derived from the lidar surface models provide an opportunity to test these observations. The results of this analysis, conducted on the north

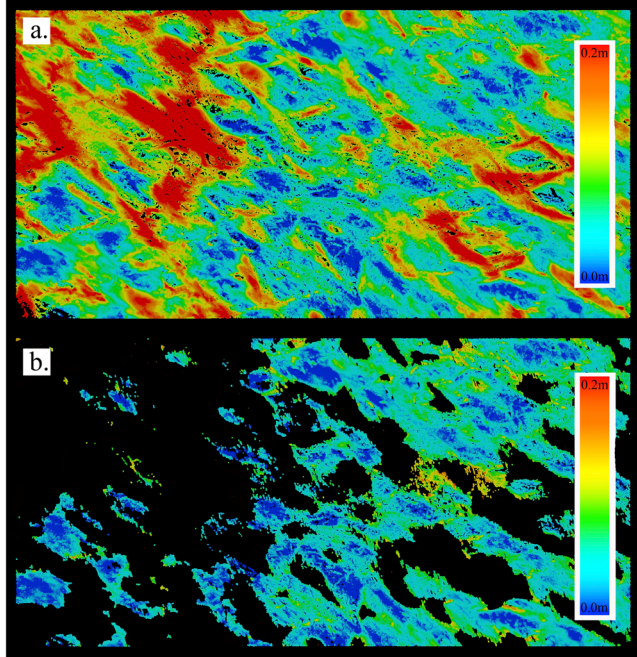


Figure 8. Height colored premelt surface map of (a) entire 2009 north site on 28 May and (b) just those areas which become pond covered on 7 June. Higher areas are hot colors and lower areas are cool colors. Full scale is 0.2 m. The areas which become pond covered are dominated by low premelt elevations.

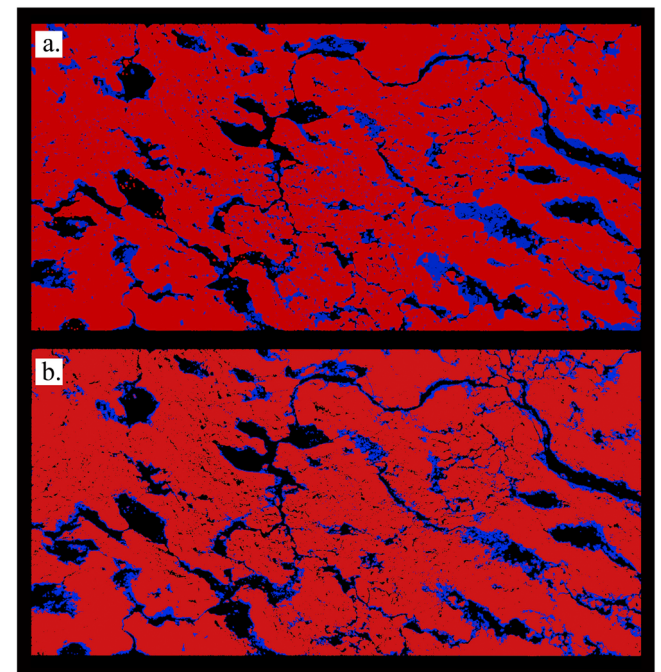


Figure 9. A comparison between pond growth locations and areas of low surface elevation. (a) Ice surface on 13 June 2009 at the north site with all areas where ponds form between 13 June and 23 June highlighted in blue. Areas which remain bare ice are red and areas which remain ponded are black. (b) Ice surface on 13 June 2009, where bare ice areas that are within 7 cm of sea level are highlighted in blue. Bare ice higher than 7 cm is red, and ponds are black. There is a very strong spatial correlation between pond growth locations and low initial surface elevation.

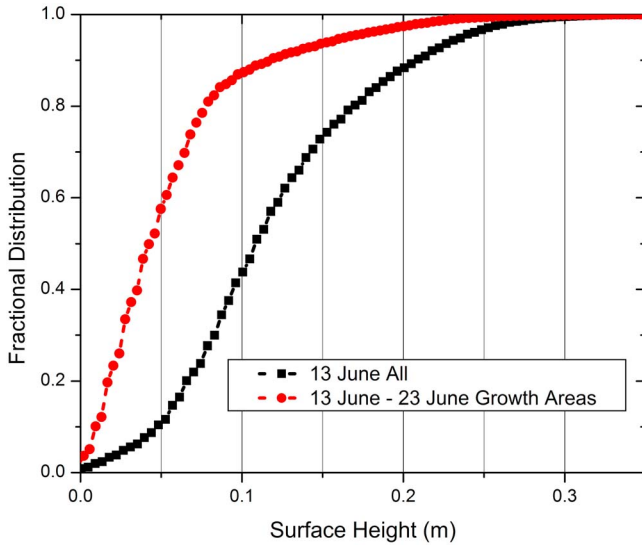


Figure 10. Cumulative surface height distribution at 2009 north site of entire surface on 13 June and of just those areas where ponds grow between 13 June and 23 June.

observation site in 2009, are plotted in green on Figure 12, along with dashed vertical lines demarcating the three stages of pond evolution. The data show that the total amount of meltwater lost from the surface of the ice is near zero for several days after the melt ponds form. Though snow and ice are being converted to liquid water, there is very little, if any, outflow during stage I. All outflow pathways appear to be shut down.

[39] Meltwater loss begins abruptly on 8 June, coinciding with the start of pond coverage decline (stage II) and the first observations of macroscopic flaws draining meltwater in the area. Though the timing of the holes' appearance suggests that the lost meltwater drains down them, we measured

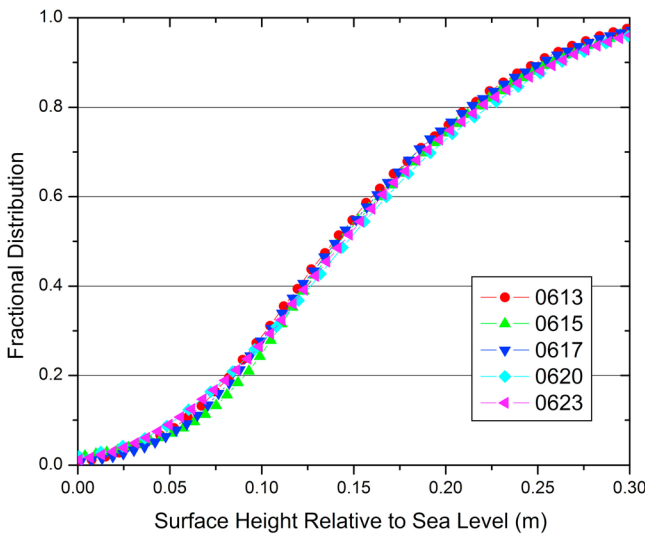


Figure 11. Cumulative surface height distributions between 13 June and 23 June showing little changed availability of surfaces within 5 cm of sea level available for flooding by an incremental drop in freeboard.

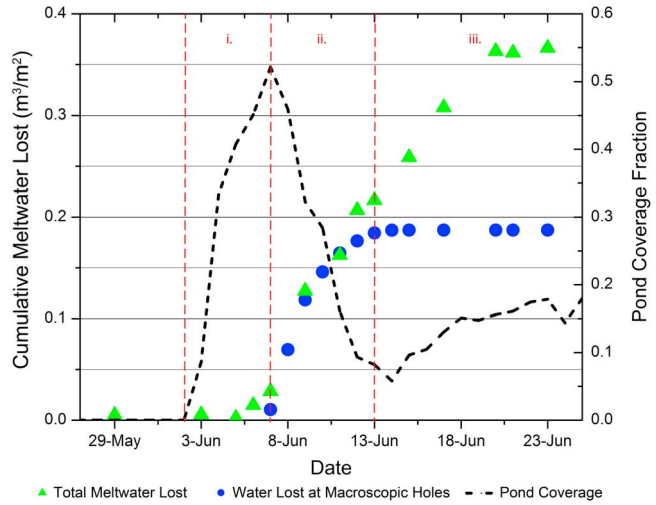


Figure 12. Total meltwater lost from the surface of the ice and meltwater measured flowing down macroscopic holes are plotted with pond coverage. The meltwater loss is presented as a cumulative of volume water lost per unit area in m^3/m^2 , equivalent to a depth of water in m. Markers i, ii, and iii denote the stages of pond evolution. The dashed red line to the left of i marks the start of pond formation, the one to the left of ii marks the date macroscopic flaws appear, and the one to the left of iii marks the date pond level becomes very nearly sea level.

outflow at the holes to determine whether percolation through the ice was also active. The 2009 north observation site provided an opportune site for this study because it was located within a closed hydraulic basin defined by a low ridge. Combined with the lack of significant precipitation during this time ($<1 \text{ cm}$ water equivalent), and minimal expected evaporation ($rH > 90\%$, $T = \sim 0^\circ\text{C}$), the features of this site allow us to make a direct comparison of the amount of water measured flowing down the holes in the basin to the lidar-derived total meltwater loss. Because they are collected over different areas (the entire floe versus just the lidar field), both measurements are converted to a water volume per unit area (water depth) and plotted in Figure 12 on a cumulative basis for comparison. The two curves track one another closely during stage II, indicating that the vast majority of the meltwater lost from the surface of the ice is accounted for by flow down the macroscopic drainage holes. The ice, therefore, remained largely impermeable to percolation during stage II and the reduction in pond coverage was controlled by horizontal transport of meltwater over the ice surface to macroscopic flaws.

[40] As we move into stage III, however, and the ponds drain down to very near sea level, the water loss measured at the holes (blue) no longer accounts for the total amount of meltwater being lost (green). Soon meltwater flow at the holes stops altogether. The plot in Figure 12 shows that during this third stage approximately 20 cm ($0.2 \text{ m}^3/\text{m}^2$) of water equivalent was lost from the ice surface (green) but only about 3 cm ($0.03 \text{ m}^3/\text{m}^2$) of this was accounted for by meltwater flowing down the holes (blue). Because meltwater continues to be lost from the surface of the ice rapidly, and evaporation is still expected to be very minimal, the process

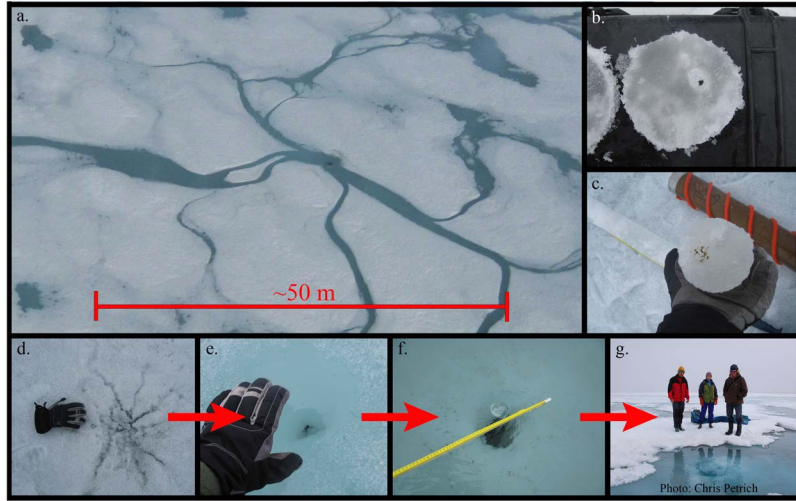


Figure 13. Composite of photos showing the evolution of brine channels to macroscopic drainage holes.

of elimination suggests that the meltwater is instead lost by percolation through the ice. This may be occurring through the bare ice, where newly created meltwater still has significant hydraulic head to drive the percolation, or through pond bottoms if permeability reaches levels high enough that the very small hydraulic potential which remains in the ponds could force sufficient water loss by percolation; either is plausible. Previous work has shown that apparent ice permeability changes from immeasurably small (permeability constant, $k < 10^{-12}$) to summertime values of between 10^{-11} and 10^{-9} over a period of about a week [Eicken et al., 2002]. By applying Darcy's law with values for the permeability constant in the range measured for summer ice, we can show that the amount of water lost during stage III (about 1.4 cm/day or $0.014 \text{ m}^3/\text{m}^2$) could be forced through the ice by very small hydraulic head, of between 0.03 mm and 3 mm

$$Q = \frac{-kA}{\mu} \frac{(\Delta P)}{L}, \quad (5)$$

where Q is the flow rate, k is the permeability constant, A is the area of flux, ΔP is the pressure head, L is the thickness of the ice (nominally 1 m), and μ is the dynamic viscosity of the water: $\mu = 1.787 \times 10^{-3} \text{ N s/m}^2$.

[41] Small gradients in the pond surfaces caused by wind-forcing or inflow in areas far from one of the macroscopic holes can easily create a head of this magnitude without driving large horizontal transport.

[42] This calculation, combined with meltwater balance data suggests that the ice may have undergone a rapid permeability transition, similar to that observed by Eicken et al. [2002], over the 2–3 days centered on 13 June, allowing percolation through the ice to become the primary means of meltwater loss in stage III, despite very low hydraulic head in the ponds. This hypothesis is supported later by evidence from ice core observations.

4.3. Interactions of Meltwater With Ice

[43] The analysis of meltwater flows confirms the power of hydraulic controls on the pond evolution and provides

insight into relative importance and the timing of transitions between outflow mechanisms. This information enables the identification and further exploration of the mechanisms of ice and meltwater interaction which caused the appearance of drainage flaws and the apparent permeability transition.

4.3.1. The Formation of Flaws From Brine Channels

[44] Each year of our study, the macroscopic flaws, implicated as the cause of pond coverage decline in stage II, were not observed until the first day of melt pond decline, and seemed to spontaneously arise between daily visits to the site. During 2009, sequential daily aerial photos presented additional evidence of the holes' sudden appearance. The first holes observed from the ground were readily visible in aerial photographs taken on 8 June, but absent in photos taken the day before, prompting us to explore their origin. Seals were present at some of the holes, suggesting that they were breathing holes kept open through the winter, as others have concluded when observing similar drainage features [Barber and Yackel, 1999; Holt and Digby, 1985]. The seal holes are even known to have a protective dome of ice and snow through the winter which the seals often remove in order to haul out for basking behavior necessary to molt at this time of year (B. Kelly, personal communication, 2009), potentially explaining a sudden appearance.

[45] Indeed some of the very first holes noted were likely seal holes, as seals have been documented in previous years maintaining breathing holes through the ice within the study area [Kelly, 1996]. Over the next several days, however, the number of holes visible in aerial photographs (e.g., Figure 13a) and confirmed from ground observations grew rapidly. Based on conversations with local Inupiat hunters, such as G. Mongoyak and B. Adams (personal communications, 2009), we determined that the number of holes observed greatly exceeded the expected density seal breathing holes. Similar densities of holes were present in aerial photos taken up to 100 km offshore, indicating that the phenomenon driving hole formation was regionally ubiquitous. Throughout stage II, while meltwater level in the ponds remained above sea level, holes appeared each day where they had not been noted the previous day. New holes widened in proportion to their flow rate, reaching diameters as

large as 2 m, but more typically 0.5 m. We observed similar widening with man-made holes created when cores were taken from ponds at our coring sites. More interesting, however, was the observation that the smallest holes found were under 5 cm in diameter. The small size, combined with the sheer number of holes found, over 100 per km² by 16 June, indicated the origin of the vast majority of the holes was unlikely to have been related to the seals.

[46] Instead, organized brine drainage channels, which have long been known to form during ice growth to reject brine [Lake and Lewis, 1970], were identified as a potential origin of the majority of the holes. These features were observed preferentially melting at the surface in many places, (Figure 13d) and evolving into tiny connective holes (Figure 13e). We hypothesized that as ice temperatures increased the brine volume in these channels would increase, until they became connected from the surface to the ocean, allowing meltwater to begin flowing down them. Once flow began, heat transfer from the moving water rapidly widened the hole, just as it did for holes drilled in the bottom of a pond at our coring site (Figures 13f and 13g). Several of the non-connective brine drainage channels visible at the surface were removed in ice cores to observe the development prior to connectivity. In these cores, we were easily able to identify the bottom of the channels due to enhanced algal growth (Figure 13c). Horizontally sectioning the cores in the field allowed us to follow the open, 0.25–0.75 cm diameter brine drainage holes (Figure 13b) most of the way through the ice. The exception was a portion about 0.65 to 0.85 m below the surface in 1.05 m thick ice which corresponded with the coldest part of the ice ($T = -0.9^{\circ}\text{C}$) and where the channel could not definitively be seen. We hypothesized that these non-connective channels had actually become plugged with refreezing meltwater, a theory that we explore in detail below.

4.3.2. The Permeability Transition

[47] Though flaws forming from brine channels controlled meltwater drainage in stage II, the meltwater balance data show that the predominant mode of meltwater loss transitioned to percolation during the beginning of stage III. The rapidly increasing volume of water lost to percolation during the transition, despite dropping hydraulic head, indicates that the increase in ice permeability was rather abrupt. Mechanisms suggested for causing such a transition in ice permeability include reaching a porosity threshold above which pore connectivity rapidly increases (percolation theory) [Golden, 2001; Fetterer and Untersteiner, 1998], the destruction of a surface layer of impermeable superimposed ice formed during snowmelt [Eicken et al., 2004], and the destruction of a layer of ice in which the pores have been plugged by the formation of interposed fresh ice [Freitag and Eicken, 2003]. Our knowledge of the timing of the permeability transition, combined with simultaneous measurements of ice properties, provides an opportunity to examine each of these mechanisms.

[48] One application of percolation theory to ice makes a clear prediction that the ice should undergo a permeability transition at about 5% brine volume [Golden, 2001]. Ice porosity, p , presumed to be equivalent to the brine volume, was calculated in our experiment according to (6), using salinity and temperature profiles collected from ice cores and

embedded thermistor strings [Frankenstein and Garner, 1967]

$$p = S \left(0.0532 - \frac{4.919}{T} \right), \quad (6)$$

where S is salinity in psu, T = temperature in $^{\circ}\text{C}$, and p = % porosity.

[49] Dated vertical profiles of calculated porosity from prior to the onset of ponding can be found in Figure 14b. Comparing the data to a 5% brine volume percolation threshold (marked as a vertical line) shows that the entire profile of the ice exceeded the percolation threshold during the first weeks of May, about six weeks prior to the observed onset of meltwater percolation, and a month prior to the initial formation of ponds. Ice salinity profiles, shown in Figure 14a, begin to show freshening in the uppermost layers of the ice at this time, indicating the start of brine gravity drainage and the onset of ice permeability, as expected from theory. Because brine movement occurs even in the upper, granular, ice layers, which are believed to have a higher percolation threshold due to less organized brine inclusion structures [Golden et al., 1998], the entire ice column has passed through its porosity-based percolation threshold.

[50] These observations support the application of percolation theory to predict a sea ice permeability transition based on pore connectivity. Timing clearly indicates, however, that the initial, temperature dependent increase of porosity through the percolation threshold is not the mechanism responsible for the onset of meltwater percolation through the ice.

[51] The formation of either superimposed or interposed fresh ice could provide a means to prevent percolation through an ice cover with high bulk porosity. Superimposed ice, defined here as a discrete layer of refrozen snowmelt forming on the surface of the ice, was observed extensively in all three study years. Qualitatively, the superimposed ice layer was of highly variable thickness. Clearing the snow from the ice after the onset of snowmelt, but prior to pond formation, showed a bumpy layer of newly accreted ice consistent with spatially heterogeneous percolation of meltwater through the snow. The layer's thickness was highly dependent on snow depth, averaging up to 8 cm thick beneath 40 cm deep snow dunes, but less than 4 cm thick and often absent entirely in areas of thin snow cover which would later be the sites of melt ponds. Beneath snow dunes, superimposed ice was sometimes thick enough to be identified in cores taken after the onset of ponding. The extremely fresh superimposed layer typically yielded substantially lower porosity, as derived from temperature- and salinity-determined brine volume, than the rest of the ice; often below the 5% percolation threshold. The use of brine volume as a proxy for porosity, however, may not be valid in the case of superimposed ice, where substantial bubble fraction is trapped. This higher bubble fraction made superimposed ice easy to identify in pond bottoms, from which the superimposed ice layer was observed to separate 2–5 days after ponding in large, highly porous sheets 2–4 cm thick (see image in Figure 15). We tracked the presence of this layer visually in the bottoms of the melt ponds, characterizing ponds along the transects as being lined with either superimposed

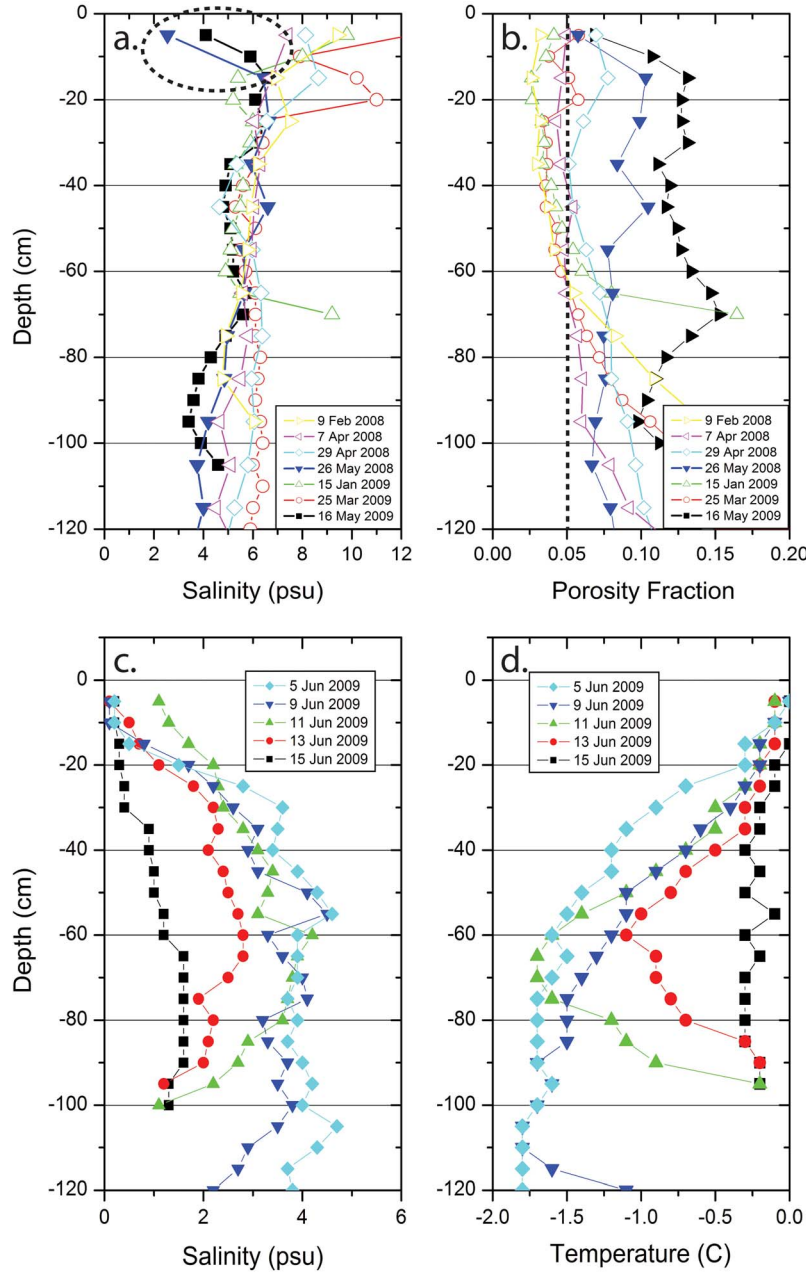


Figure 14. Profiles of (a) salinity and (b) calculated porosity from ice cores in late winter and early spring. Freshening in the upper ice (dashed oval) during May corresponds temporally to increases in porosity above 5%. Data are from the Barrow Ice Observatory (<http://seacie.alaska.edu/gi/observatories>). Profiles of (c) salinity and (d) temperature in ice cores taken later in the melt season beneath ponds. Note gradual freshening in the upper ice layers until the onset of percolation about 13 June, when salinity begins to drop throughout the ice column, indicating flushing.

ice or sea ice. The percentage of pond bottoms free of superimposed ice in 2009 is plotted in Figure 16. Superimposed ice began to break free of the pond bottoms on 5 June, and nearly all pond bottoms were free of superimposed ice by 9 June, about 3 days before the permeability transition. The timing of the gradual loss of superimposed ice several days earlier than the permeability transition, indicates that superimposed ice removal is likely not the cause of the permeability transition.

[52] Another smaller basin which we monitored in 2009 helps to further demonstrate this point. The basin, pictured in Figure 17, did not develop a macroscopic flaw until 11 June and exhibited no net loss in meltwater equivalent, inferred from lidar, well after the rest of the ice had begun draining. The pond within the basin both deepened and widened until, on 11 June, it drained in a matter of hours down a macroscopic flaw which formed in the bottom of the pond. By that time, all of the snow, and more than 20 cm of the sea ice on

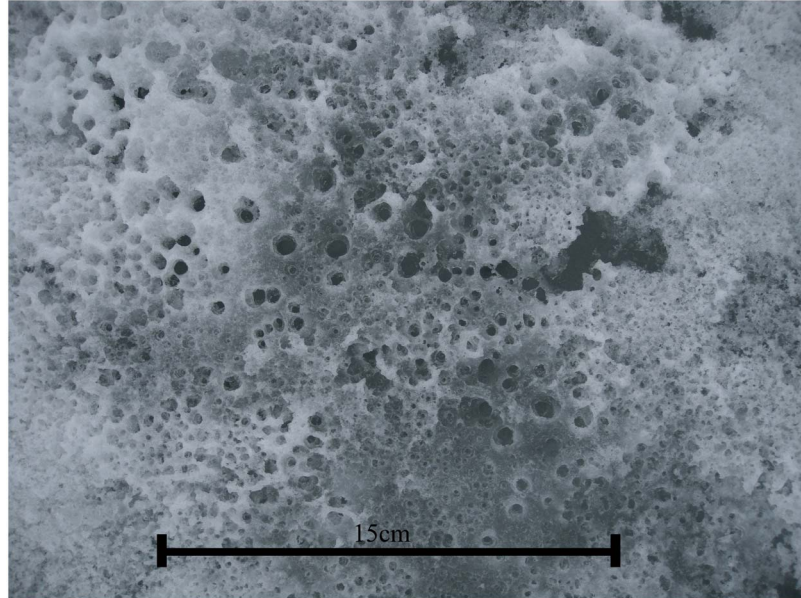


Figure 15. Image of highly porous melting superimposed ice breaking away from pond bottoms on 7 June 2009.

the bottom of the pond had ablated, according to fixed ablation stakes within the pond. The superimposed ice layer had clearly been removed, while the ice remained quite impermeable. Though superimposed ice was observed to form, and may or may not be impermeable, its removal did not trigger the permeability transition at the start of stage III.

[53] There is substantial evidence in our data supporting the notion that fresh meltwater refreezes as it intrudes into brine filled pore structure within the ice to form interposed ice plugs. When meltwater begins to pool on the ice surface in early June, both percolation theory and our observations of brine gravity drainage suggest that connective pathways exist for water to percolate into the ice. Profiles of temperature and salinity taken during melt (Figures 14c and 14d) show desalination to increasing depths in the upper ice during stage I and II of pond evolution, indicating that brine is being flushed from the upper pores by intruding meltwater. Deeper down, within the colder parts of the ice, however, salinity remains nearly constant, indicating that fresh meltwater is not free to flush through the colder ice, despite its high porosity. The limited penetration of meltwater during stage I and II can be confirmed by stable isotope measurements because the meltwater, composed substantially of snowmelt, is highly depleted in heavy isotopes. Vertical profiles of stable isotopes (Figure 18), taken beneath melt ponds during stage I and II, confirm the presence of substantial amounts of meteoric water up to 30 cm into the upper ice, even beneath layers of superimposed ice. In contrast, a profile collected during the permeability transition that occurs at the start of stage III no longer shows meteoric water in the upper ice and captures some light isotopes deep in the ice. Though it is unclear if the core captures meltwater which is still draining deeper into the ice from above or meltwater convecting upward from below ice melt ponds [Eicken et al., 2002], the flushing of light isotopes from the upper part of the ice indicates that free movement of fresh water has begun.

[54] Despite the freshening that occurs as meltwater penetrates into the upper ice, the sea ice porosity beneath ponds, derived from bulk salinity and temperature of cores, remains well above the percolation threshold of 5%, even at the depths where we expect ice plugs must be forming. We hypothesize that this apparent contradiction of percolation theory occurs because the formation of interposed ice happens preferentially in the most critical connective pathways. As meltwater plumes percolate downward in tortuous, connective pathways, the meltwater will begin to freeze to the walls of the pores when cold ice is encountered. Given similar rates of accretion on all walls, constricted points

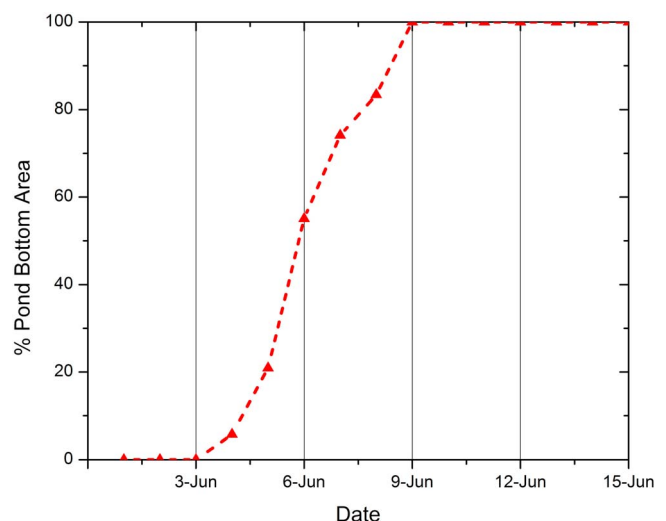


Figure 16. Percentage of all ponds along transects lined with superimposed ice versus date. Superimposed ice is removed several days prior to the onset of percolation on 13 June.

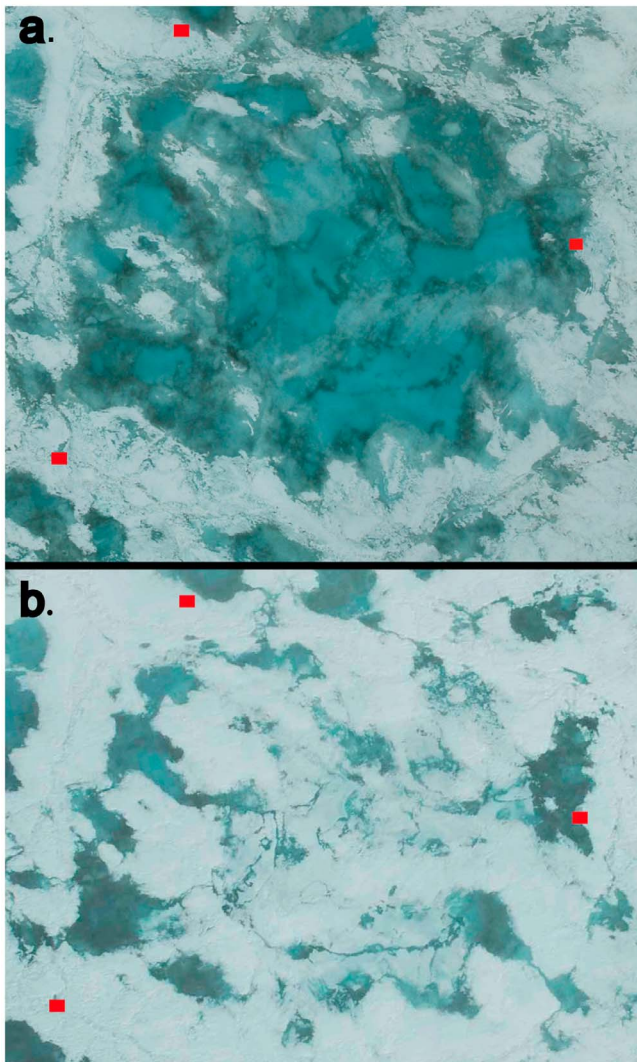


Figure 17. Aerial photos of a small basin taken on (a) 10 June and (b) 13 June. Lidar observations on the morning of 11 June showed that drainage had barely begun and the scene looked very similar to 10 June, while by the evening the scene looked essentially as it did on 13 June when the second picture was taken.

along the pathway that the water propagates would be expected to fill with ice most rapidly, while larger pores may not entirely refreeze. If such constriction points exist, a small volume of ice could stop percolation without significantly altering the bulk salinity of the ice, as measured by our 10 cm diameter coring. By selectively blocking critical connections between the pores, however, the refreezing meltwater would alter the expected relationships between bulk porosity and pore connectivity which percolation theory depends upon.

4.3.3. The Linkage Between Percolation and Flaw Formation

[55] We propose that both the formation of interposed ice and the widening of brine channels are a single process dependent on the initial size of the pore into which meltwater flows. When fresh meltwater intrudes from above into a brine-filled pore, it displaces the brine downward and

comes into contact with ice which is below its freezing point, causing the meltwater to freeze. The meltwater delivers heat to the inside of the pore by giving off latent heat as it freezes, carrying small amounts of specific heat, and frictionally dissipating even smaller amounts of kinetic flow energy. Whether a hole will freeze shut and form a fresh ice plug or widen as the meltwater delivers energy depends entirely on the integrated energy balance at the pore wall. Several variables affect this balance, including the temperature and salinity of the ice and meltwater, the hydraulic potential of the meltwater, and the size of the pore. At a particular time in the melt season, temperature, salinity, and hydraulic head are fixed, leaving pore size as the only free variable.

[56] Brine inclusions in the ice are expected to exist in a range of sizes and, because they are formed by two distinct mechanisms, likely have a bimodal distribution. The first mechanism of brine inclusion, entrapment of brine between interconnecting ice lamellae as the ice solid fraction increases, results in brine inclusions smaller than lamellae spacing, or typically less than 1 mm in horizontal diameter [Perovich and Gow, 1996]. The second mechanism, gravity drainage of brine during ice growth, results in organized arborescent brine channels of diameter that can greatly exceed lamellae spacing. These form as dense brine is collected and drains along a preferred pathway from the smaller inter-lamellar inclusions [Lake and Lewis, 1970]. The few available estimates place brine channel size at 1 cm or a bit less [Golden, 2001; Lake and Lewis, 1970]. The sizes of both inclusion types likely vary considerably and are dependent on temperature, however it is reasonable to expect that brine channels are roughly an order of magnitude larger than inter-lamellar inclusions. As the ice warms, we expect there would be a time at which meltwater flowing into large pores, such as well organized brine drainage channels, will enlarge the pores into macroscopic drainage holes, while meltwater flowing into smaller pores will simply refreeze, blocking them. Simple observations confirm this general concept. Large, 10-cm diameter core holes drilled through ice in the bottoms of melt ponds are simply too large to repair and widen rapidly as meltwater whirlpools into them. Much smaller, 2-mm diameter holes, drilled in a laboratory grown block of saltwater ice, self-repaired when fresh water at 0°C was poured down them at ice temperatures of up to -0.4 C.

4.3.4. Brine Channel Flow Model

[57] We created an enthalpy based model of an idealized brine drainage channel to explore the interactions of meltwater with brine channels further. Our 2D model representing a single, isolated, cylindrical brine tube consists of stacked annular cells of uniform radial thickness which retain constant volume throughout the model run. The center cells are initialized as a cylindrical tube of liquid brine, while the surrounding ice cells are initialized with temperature and salinity measured in cores taken at our site at several points during the melt season. The ice component of the model uses methods very similar to those employed in a 1D ice model by Notz and Worster [2006], tracking two primary variables, enthalpy and salinity for each gridcell, at each timestep. Enthalpy and salinity are related to secondary variables temperature and brine volume by assuming that all brine in ice-containing grid cells exists at its salinity-controlled freezing point. The concentration of the liquidus brine, S_{brine} , is calculated for a given temperature, T , by treating

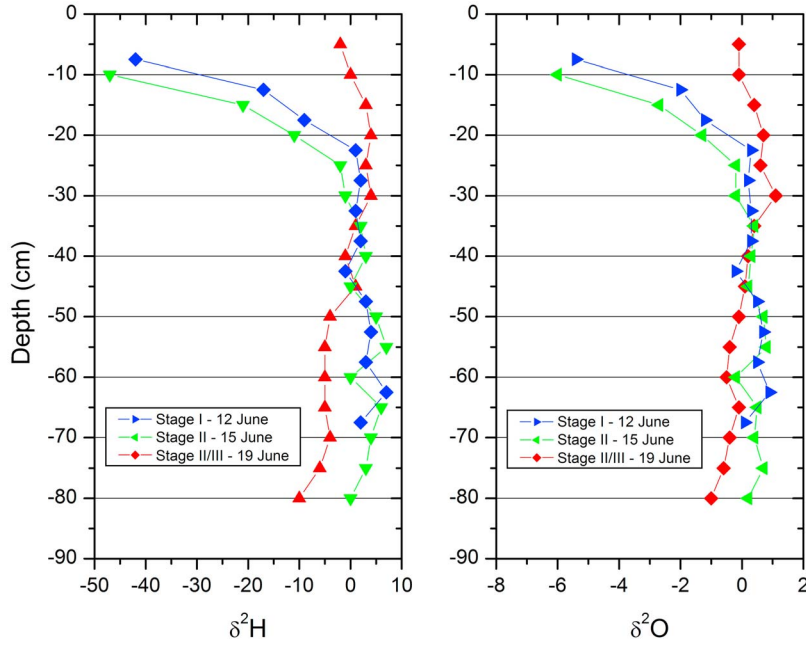


Figure 18. Profiles of $\delta^2\text{H}$ and $\delta^{18}\text{O}$ stable isotopes taken in 2010 from cores beneath melt ponds.

freezing point depression as a colligative property controlled by the cryoscopic constant of water, $k_{\text{cryo}} = 1.853 \frac{\text{K} \cdot \text{kg}}{\text{mol}}$ [Aylward and Findlay, 2002; Chang, 2007], so that

$$S_{\text{brine}} = -T \frac{\bar{M}}{k_{\text{cryo}}}, \quad (7)$$

where we use an average weight of sea salt ions, $\bar{M} = 31.41 \text{ g/mol}$ [Barnes, 1954; Bromley, 1968] to convert from salinity in psu to ion molality. This enables brine volume, v_b , and the freezing point of the cell, T_f , to be determined using bulk salinity, S_{bulk}

$$v_b = \frac{S_{\text{bulk}}}{S_{\text{brine}}} \quad (8)$$

$$T_f = S_{\text{bulk}} \frac{k_{\text{cryo}}}{\bar{M}}. \quad (9)$$

[58] The enthalpy of each cell, H , is related to temperature and salinity according to the changes in both specific and latent heat required to reach the current brine fraction and temperature from the reference state, where $H_{\text{ref}} = 334 \text{ J/g}$ at $T = 0^\circ\text{C}$, fully liquid

$$H = (1 - v_b)L - c_l T_f + v_b c_l (T - T_f) + c_s (1 - v_b)(T - T_f), \quad (10)$$

where the first term represents the latent heat (L) required to freeze the solid fraction, the second term represents the specific heat required to cool the water to its salinity determined freezing point, T_f (in Celsius), and the third and fourth terms represent a simple approximation for the specific heat required to cool the brine and solid fractions from the freezing point to the current temperature (T). In the equation, c_l and c_s are the liquid and solid heat capacities, $4.2 \text{ J/g} \cdot \text{K}$ and $2.1 \text{ J/g} \cdot \text{K}$ respectively.

[59] Radial heat transfer \dot{H} is calculated at each time step according to Fourier's law of heat conduction in cylindrical coordinates [Fourier, 1822; Kakaç and Yener, 1993]

$$\dot{H} = -k A_r \frac{dT}{dr} = -2k\pi r l \frac{dT}{dr}, \quad (11)$$

where the conductivity of the cells, k , is calculated as a weighted average of constant solid and liquid conductivities based on the brine volume

$$k = k_l v_b + k_s (1 - v_b), \quad (12)$$

with $k_l = 0.58 \frac{\text{W}}{\text{mK}}$ and $k_s = 2.0 \frac{\text{W}}{\text{mK}}$ [Incropera and DeWitt, 2007].

[60] Heat transferred into or out of a cell is added to each cell's enthalpy value, and new temperatures, brine volumes, and conductivities are calculated from the updated enthalpy values to begin the next time step.

[61] Meltwater flowing into the brine channel has a fixed temperature and salinity of 0.1°C and 1.5 ppt, based on measurements of these taken in ponds which had not yet melted through to the ocean. Hydraulic head is set to 0.2 m, representative of an average head immediately prior to the formation of drainage flaws.

[62] Fluid flow rate and heat transfer within the brine tube are approximated by two regimes based on Reynolds number of flow

$$\text{Re} = \frac{Vd}{v}, \quad (13)$$

where V is the velocity, in m/s of the flow, d is the pipe diameter, and v is the kinematic viscosity of water at 0°C . Reynolds number below 2300 indicates laminar flow, while flow with Reynolds number above 4000 is considered turbulent [Eckert and Drake, 1959]. The tube lengths and head height used in our model result in a turbulent Reynolds

number for channel diameters greater than roughly 4 mm. Intermediate Reynolds numbers are considered transient. Flow volume in the transient state is calculated from an interpolation of the mechanisms, while heat transfer is assumed to be strictly conductive as in laminar flow.

[63] For laminar and transient flow, volumetric flow rate is calculated using the Hagen-Poiseuille pipe flow relationship [Eckert and Drake, 1959; Shams, 1992]

$$Q = \frac{\Delta P \pi r^4}{8\mu L}, \quad (14)$$

where pressure difference is calculated from water density, gravitational constant, and hydraulic head, $\Delta P = \rho gh$, r is the tube radius, L is the tube length, and μ is the dynamic viscosity of water, $\mu = 1.787 \times 10^{-3} \frac{Ns}{m^2}$ [Eckert and Drake, 1959].

[64] In the turbulent regime, flow rate is calculated from conservation of energy by equating kinetic energy and frictional loss of the flow to available potential energy (PE) and deriving an expression for flow velocity in terms of hydraulic head and channel diameter

$$PE = \dot{m}hg = \frac{1}{2}\dot{m}V^2 + \dot{m}gh_f, \quad (15)$$

where \dot{m} is the mass flow rate of water, h is head, g is gravitational constant, V is velocity, and h_f is the frictional head loss during flow, calculated using the Darcy-Weisbach equation [Shams, 1992]

$$h_f = f \frac{l}{d} \frac{V^2}{2g}, \quad (16)$$

where l is the length of the tube, d is its diameter, V is the flow velocity, g is the gravitational constant, and f is the friction factor, which is dependant on the tube roughness and Reynolds number. Determining f explicitly requires a more detailed knowledge of the surface roughness within a brine channel than is available, however the value of f is not particularly sensitive to assumed pipe roughness or Reynolds number; varying over a range of ~ 0.2 – 0.4 for the full range of relative roughness values found in typical pipe flow problems and the range of Reynolds numbers modeled here [Shams, 1992]. In order to improve the estimate of flow rate from the frictionless case, where $h_f = 0$, we assume a relatively smooth tube wall, with relative roughness = 10^{-4} and calculate f from a Moody diagram [Moody, 1944; Shams, 1992] using the Reynolds number of the frictionless flow velocity $v = \sqrt{gh}$. Substituting h_f into equation (15) allows for derivation of V

$$V = \sqrt{\frac{hg}{\frac{1}{2} + \frac{f}{2d}}}. \quad (17)$$

Volumetric flow rate is then calculated by multiplying flow velocity by pipe cross section.

[65] Radial heat transfer in the liquid is modeled by simple heat conduction for the laminar and transient flow cases in the same manner as for the ice component. Enhanced radial heat transfer due to mixing in the turbulent regime is calculated using a convective heat transfer coefficient derived

from the Dittus-Boelter correlation [Incropera and DeWitt, 2007]

$$\dot{H} = hA\Delta T, \quad (18)$$

where heat transfer coefficient $h = (k_l/d)Nu$, Nusselt number is derived from Reynolds and Prandtl numbers, $Nu = 0.023 Re^{0.8} Pr^{0.33}$ [Incropera and DeWitt, 2007; White, 2006], A is the area of transfer surface, and ΔT is the temperature difference between the transfer surface and the fluid temperature.

[66] Salinity within the ice very near (cm scale) the channel is expected to decline when fresh water begins to flow down the channel, as brine within adjacent, connected pockets diffuses, convectively mixes, and becomes entrained in the freshwater flow. This expected desalination was qualitatively observed by taking salinity core samples immediately adjacent to developing holes. The rate of this desalination is important to the model because it lowers the calculated effective heat capacity of the ice near the channel. Lacking sufficient data to constrain this desalination at high resolution, we set the model to run three cases. Two cases bound the result with no desalination and immediate and complete desalination of the surrounding ice while a third, best-estimate case allows desalination by simple diffusion. Actual desalination is most likely greater than simple diffusion. In all cases, fresh ice is presumed to form on the interior of the tube if ice growth occurs. Vertical heat conduction and solar energy deposition are neglected due to the relatively short period of time required for a given diameter channel to either enlarge or freeze. Viscous dissipation as a heat source within the channel is ignored because the total potential loss of the water (head height times mass flow times gravity) distributed evenly along the channel wall is at least an order of magnitude smaller than that conducted from the incoming water.

4.3.5. Model Results

[67] When run with a range of initial flaw diameters in a fixed ice profile, the model results show the strong threshold behavior with respect to channel diameter expected. The results of such a test are plotted in Figure 19, where the minimum channel diameter is tracked over time for various starting diameters. Channels initially below a critical diameter, here 1.5 cm, rapidly close when ice begins to form on the channel walls, slowing meltwater flow and causing a negative feedback that allows thermal conduction into the ice to increasingly exceed energy delivery. Only slightly above that critical diameter, the channel begins to close, but thermal conduction into the ice slows as the ice is warmed, dropping below the rate of heat delivery from the meltwater before the channel can be closed completely. Once energy delivery exceeds conduction, the channel begins to widen and a positive feedback sets in. The ratio of cross-section-dependent flow rate to circumference-dependent heat conduction increases the net heat flux to the channel walls while the ice warms and conduction slows. The result is a steady widening of the hole despite the increasing ice volume that must be melted for a given diameter increase as the hole widens.

[68] Predictions of critical channel diameter, based on ice properties collected in 2009 ice cores, are plotted in Figure 20 for all three desalination schemes. The results highlight a decline in critical channel diameter which accelerates as the

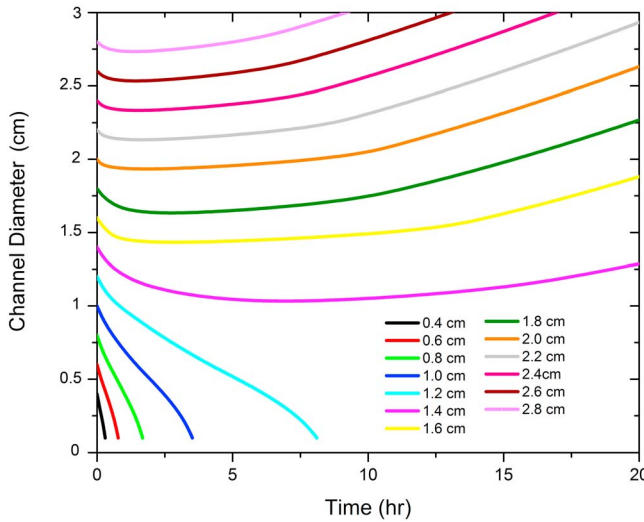


Figure 19. Minimum diameter of modeled flow channels versus time for varying starting diameters in 5 June 2009 ice temperature and salinity conditions.

ice warms during melt. At the time that drainage flaws were appearing on 8 June, the critical channel diameter predictions range from 0.8 to 1.8 cm with the three desalination schemes. This range is in quantitative agreement with the expected size of the largest organized brine drainage channels, further supporting the notion that brine channels will predictably enlarge to produce macroscopic flaws. After drainage flaws began to open on 8 June, predicted critical channel diameter begins to drop rapidly, allowing flow through smaller and smaller inclusions and suggesting that the observed permeability transition occurs because the critical diameter for percolation passes below the typical porosity size. When the permeability transition occurred on 13 June, however, predicted critical diameter is between the expected size of the two brine inclusion types, leaving the relative roles of interlamellar brine inclusions and smaller brine channels in causing the percolation transition unclear. Expected growth of the interlamellar inclusions as the ice warms may account for part of the size difference, but we also note that the observed density of brine channels in the ice, at 60–120 per m² [Golden, 2001], is much greater than the observed density of enlarged holes of roughly 100 per km². If the unaccounted for brine channels did not plug irreversibly in early melt, percolation may proceed down these channels when the critical channel diameter drops below their typical size. Clearly identifying which type of the flaw causes percolation will require more precise characterization of inclusion sizes during melt and in situ study. The model results, however, make clear the importance of temperature dependent interactions between fresh meltwater and the porosity of the sea ice in determining the availability of meltwater outflow pathways.

5. Discussion

5.1. Ponds, Albedo, and Surface Energy Balance

[69] Much of the justification for this work centers on the presumption that the temporal evolution of ponds, particularly

the highly transient early season spike in pond coverage observed, changes the albedo and therefore seasonal surface energy balance by a significant amount. The results of our field observations can be used to confirm this. The changes in integrated shortwave albedo caused by shifts in pond coverage were quite significant. Spatially averaged albedo, calculated from measurements along the transect lines, is plotted in Figure 21a. Prior to pond formation, when the ice surface is snow covered, albedo is relatively stable. Albedo varies between ~0.7 and ~0.8 depending on the age and surface temperature of the snow. As snowmelts, exposing bare ice and forming melt ponds, albedo drops significantly and begins to show greater variability. We note that albedo follows a trend inverse to that of pond coverage during each stage of pond development. Plotting albedo versus pond coverage in Figure 21b illustrates the strength of this correlation and helps to confirm that pond coverage is the primary driver of albedo changes on melting ice [Grenfell and Perovich, 2004].

[70] Despite the short duration of enhanced pond coverage during stage I and II of pond evolution, timing of these stages near peak annual insolation results in a large impact on the surface energy balance. Insolation data, collected at the DOE Atmospheric Radiation Measurement site about 4 km away, show that average solar input during the study periods was 254 W/m², with a standard deviation between daily values of 57 W/m² (Table 1). The observed spatially averaged albedo range after pond formation of ~0.25 to ~0.60 therefore translates to a range in absorbed shortwave flux of around 90 W/m². Assuming a conservatively high ice density of 900 kg/m³ and a latent heat of fusion of 334 kJ/kg, this is enough energy to melt at least 2.6 cm of ice per day. Even moderate changes in the duration of peak pond coverage could therefore have significant impacts on overall ice mass balance. Though the duration of peak pond coverage did not exhibit high variability during our three year program, spiking above 45% for only 2–4 days each year, other studies on undeformed FYI have observed much longer

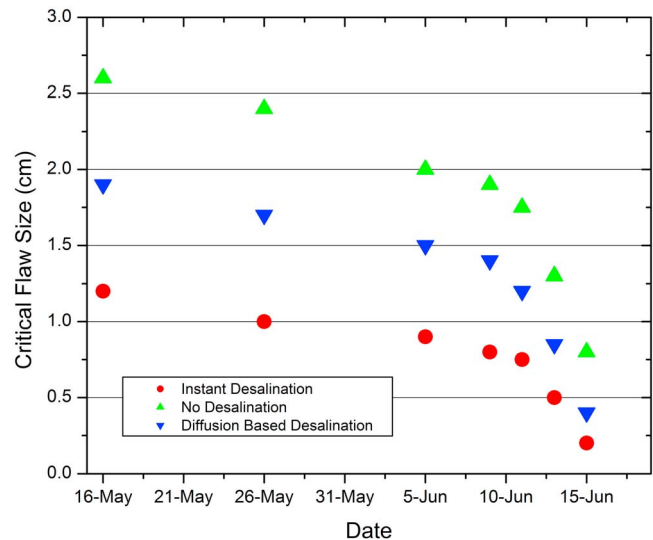


Figure 20. Critical pore diameter versus date for three desalination schemes.

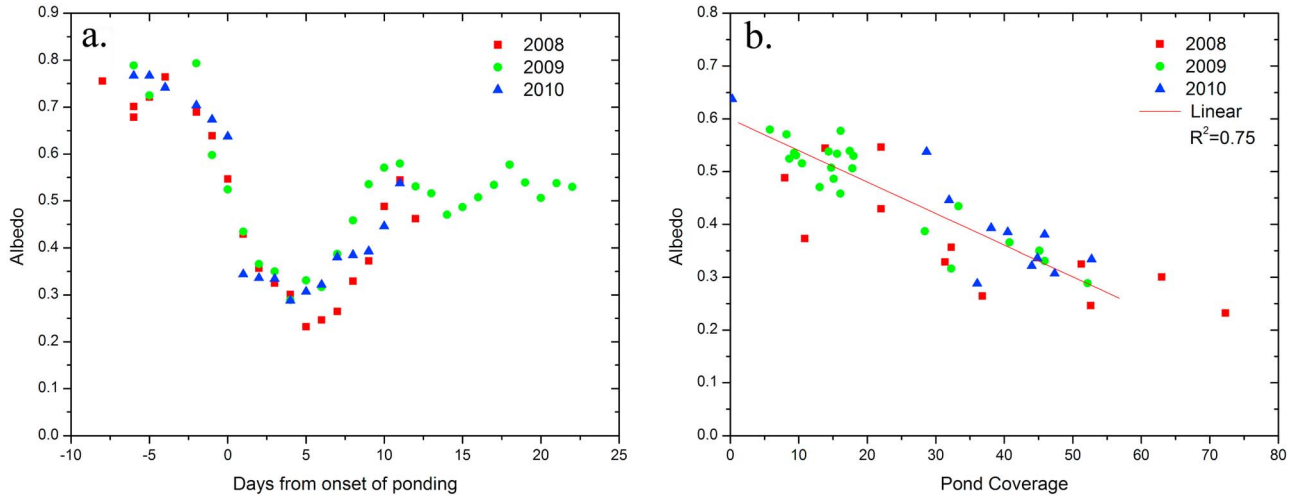


Figure 21. (a) Albedo evolution during the three years of observations. (b) Albedo versus melt pond coverage.

stage I duration, with early season pond coverage peaking in excess of 45% for 10–13 days [Scharien and Yackel, 2005; Eicken et al., 2004].

5.2. A Simple Comparison of Pond Observations to Model Parameterizations

[71] Two predictions of pond coverage, calculated based on published GCM parameterizations, are plotted with our 2009 pond coverage observations in Figure 22. The first, based on the CCSM CICE 4.0 parameterization [Hunke and Lipscomb, 2010], calculates pond coverage from meltwater generation rate, retaining 10% of the meltwater created and distributing it into ponds having a linear depth to area fraction relationship $h_p = 0.8 f_p$. The meltwater generation rate used to force the parameterization was calculated from snow and ice melt rates observed at the ablation stakes surrounding our 2009 sites. The second, based on a parameterization designed for ECHAM5 [Pedersen et al., 2009], uses the provided relationship, $f_{mp} = 0.5 * \tanh(30 d_{mp} - 2.5) + 0.5$, to relate FYI pond fraction, f_{mp} , to pond depth, d_{mp} .

[72] This parameterization is forced with average pond depth measured along the two 200 m transect lines. Each parameterization tracks part of the melt season quite well, but miss-estimates the pond fraction in another part of the melt season substantially. Compared to the pond observations,

both would produce errors in albedo, and therefore energy balance, over this first two weeks of ponding in excess of 50 MJ/m².

[73] We realize that this direct comparison has limited scope because the parameterizations represent all ice types and because they likely behave differently outside their typical forcing environment. The comparison does, however, highlight a general challenge faced by these parameterizations. Both models rely on a functional relationship to convert between pond depth and area fraction; CICE a linear function, and ECHAM a more complex function. The CICE model also relies on a functional relationship to convert between meltwater volume produced and meltwater volume retained in ponds. Our observations of these relationships (Figures 23a and 23b) show that, due to substantial topographic evolution and dramatic changes in meltwater balance during the melt season, neither of these relationships

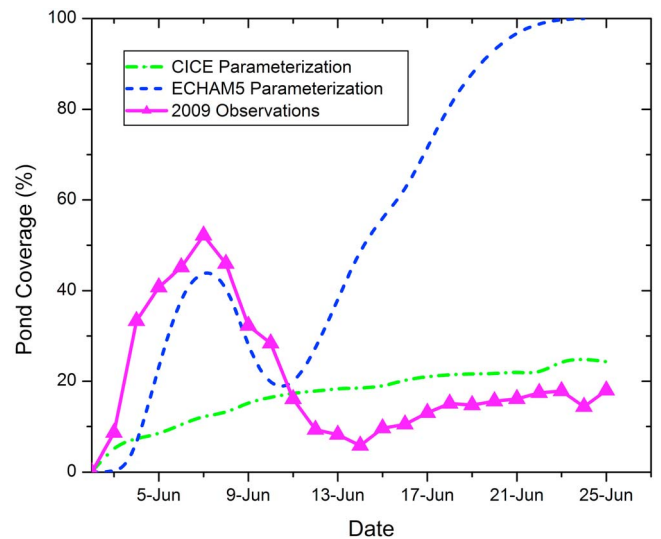


Figure 22. Comparison of observed pond coverage and GCM pond parameterizations.

Table 1. Shortwave Fluxes and Potential Impact of Albedo Variations

	Average	Daily Standard Deviation	Daily Minimum	Daily Maximum
2008–2010 solar insolation (W/m ⁻²)	254	57	135	369
Net shortwave, albedo = 0.25	191	43	101	277
Net shortwave, albedo = 0.60	102	23	54	148
Difference	89	20	47	129
Enough to melt cm of ice per day	2.3	0.5	1.2	3.3

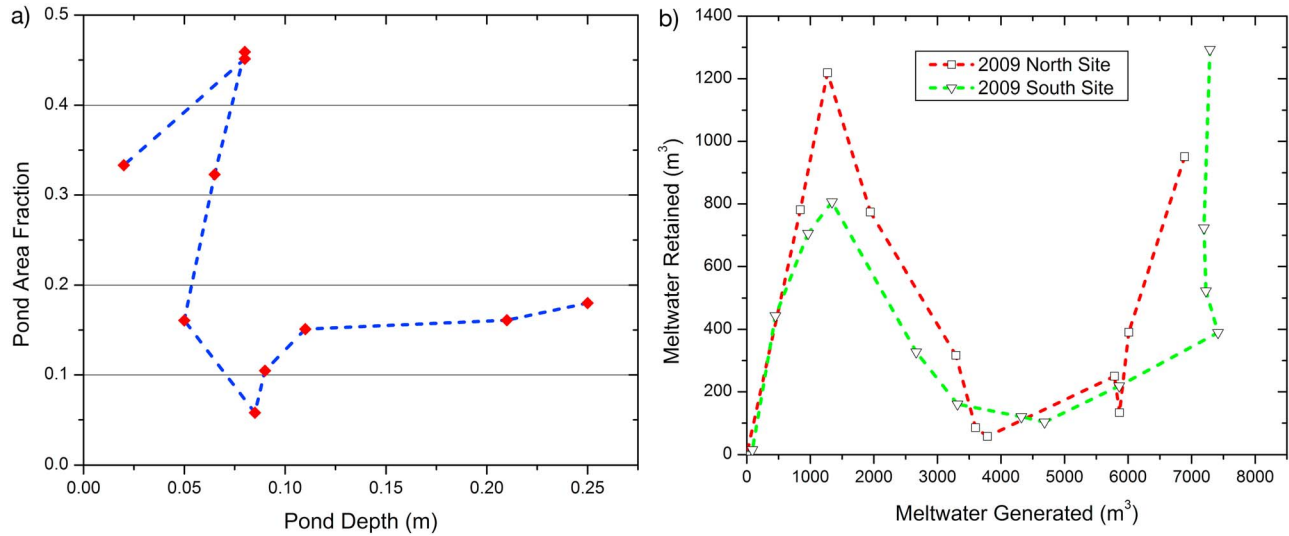


Figure 23. (a) Melt pond fraction versus average pond depth observed during 2009. (b) Total meltwater generation versus meltwater retained at the ice surface for the 2009 sites.

can be represented by a simple function, and the relationship between melt pond depth and area fraction cannot be represented by any function. For example, in Figure 23a, a pond depth of 0.07 m has three different corresponding pond fractions ranging from 0.05 to over 0.45. Improving these parameterizations will require incorporating an understanding of how these functional relationships also change with time during the melt season. A better solution still would be to relate meltwater controls to ice properties already being tracked in the GCM's, and to collect data representing the topography of various ice types to better parameterize water distribution. These observations represent an incremental step toward this goal.

6. Conclusions

[74] The summer albedo of melting Arctic sea ice is strongly affected by the fraction of the surface covered by melt ponds. Melt pond coverage varies rapidly and widely over the course of the melt season in a given place and can vary substantially from one place, or ice type, to another. Accurate albedo prediction for Arctic sea ice requires a detailed understanding of the mechanisms that force changes in pond coverage. Ice surface topography and meltwater balance are found to both play key roles in melt pond evolution. Topographic relief prior to the onset of melt, caused largely by snow dunes atop undeformed first year ice, determines the locations of initial pond formation, while the magnitude of the surface relief controls the areal extent of meltwater distribution. The temporal evolution of melt pond coverage occurs in discrete, readily identifiable stages whose transitions are controlled by the ice-temperature-dependent development of meltwater outflow pathways. During stage I, ponds form well above sea level. The ice is found to be impervious to meltwater percolation and generally free of macroscopic flaws draining meltwater, though some meltwater would be expected to run off the edge of floes in the floating pack. The rapid drainage of meltwater that occurs as pond coverage declines during stage II is predominantly due

to horizontal transport of meltwater over the ice surface to macroscopic flaws. Though any large aperture through the ice may drain meltwater during this time, the vast majority of the meltwater was found to drain downholes formed from the enlargement of brine drainage channels by flowing meltwater. The formation of interposed ice within sea ice porosity blocks theoretically expected ice permeability during stage I and II of pond development. At the start of stage III, which is defined by practically unlimited outflow pathways, percolation begins abruptly. Pond level is fixed to very near sea level throughout this stage, while overall freeboard loss results in the steady growth of ponds by surface flooding.

[75] The formation of meltwater outflow pathways that drive the stages of pond development is controlled by interactions of fresh meltwater with brine inclusions. Our model of meltwater intruding into a brine-filled pore shows that whether a specific pore will enlarge or become plugged by refreezing meltwater is highly dependent on ice temperature, salinity and the initial pore size. The distribution of pore sizes expected within the ice allows this behavior to explain the observed temporal separation between the onset of macroscopic flaw formation and the onset of percolation.

[76] The key findings of this experiment mechanistically link the temporal evolution of pond coverage, and therefore ice albedo, to ice temperature and salinity. If coupled with detailed measurements of surface topography distribution and brine inclusion characteristics on other ice types, these results provide a promising path toward improving explicit handling of melt ponds within model parameterizations.

[77] **Acknowledgments.** The authors acknowledge Steve Ackley and two anonymous reviewers, each of whom contributed substantially to the improvement of this paper. We also gratefully acknowledge the loan and support of a TLS from Dave Finnegan, substantial field work contributions by Kerry Claffey, and able technical assistance of Bruce Elder. Ice core and surface elevation data used to validate and improve several findings was collected and generously made available on the Barrow Ice Observatory website by Chris Petrich, Hajo Eicken, and Matthew Druckenmiller, who also all collaborated most helpfully in the field. Logistical support was provided by the Barrow Arctic Science Consortium, particularly Gilford Mongayk,

Nok Acher, Michael Donovan, and Lewis Brower. This research was funded by the National Science Foundation through grant ARC-0454900 and fellowship support of the Dartmouth College Polar Environmental Change IGERT Program.

References

- Aylward, G. H., and T. J. V. Findlay (2002), *SI Chemical Data*, John Wiley, Milton, Queensl., Australia.
- Barber, D. G., and J. Yackel (1999), The physical radiative and microwave scattering characteristics of melt ponds on Arctic landfast sea ice, *Int. J. Remote Sens.*, 20(10), 2069–2090, doi:10.1080/014311699212353.
- Barnes, H. (1954), Some tables for the ionic composition of sea water, *J. Exp. Biol.*, 31, 582–588.
- Barry, R. G. (1983), Arctic Ocean ice and climate: Perspectives on a century of polar research, *Ann. Assoc. Am. Geogr.*, 73(4), 485–501, doi:10.1111/j.1467-8306.1983.tb01854.x.
- Bromley, L. A. (1968), Heat capacity of sea water solutions, *J. Chem. Eng. Data*, 13(1), 60–62, doi:10.1021/je60036a019.
- Chang, R. (2007), *Chemistry*, 6th ed., McGraw-Hill, New York.
- Derksen, C., J. Piwowar, and E. LeDrew (1997), Sea-ice melt-pond fraction as determined from low level aerial photographs, *Arct. Alp. Res.*, 29(3), 345–351, doi:10.2307/1552150.
- Eckert, E. R. G., and R. M. Drake Jr. (1959), *Heat and Mass Transfer*, 2nd ed., McGraw-Hill, New York.
- Eicken, H. W. B., I. I. I. Tucker, and D. K. Perovich (2001), Indirect measurements of the mass balance of summer Arctic sea ice with an electromagnetic induction technique, *Ann. Glaciol.*, 33, 194–200, doi:10.3189/172756401781818356.
- Eicken, H., H. R. Krouse, D. Kadko, and D. K. Perovich (2002), Tracer studies of pathways and rates of meltwater transport through Arctic summer sea ice, *J. Geophys. Res.*, 107(C10), 8046, doi:10.1029/2000JC000583.
- Eicken, H., T. C. Grenfell, D. K. Perovich, J. A. Richter-Menge, and K. Frey (2004), Hydraulic controls of summer Arctic pack ice albedo, *J. Geophys. Res.*, 109, C08007, doi:10.1029/2003JC001989.
- Fetterer, F., and N. Untersteiner (1998), Observations of melt ponds on Arctic sea ice, *J. Geophys. Res.*, 103(C11), 24,821–24,835, doi:10.1029/98JC02034.
- Flocco, D., and D. L. Feltham (2007), A continuum model of melt pond evolution on Arctic sea ice, *J. Geophys. Res.*, 112, C08016, doi:10.1029/2006JC003836.
- Flocco, D., D. L. Feltham, and A. K. Turner (2010), Incorporation of a physically based melt pond scheme into the sea ice component of a climate model, *J. Geophys. Res.*, 115, C08012, doi:10.1029/2009JC005568.
- Fourier, J. B. J. (1822), *Théorie Analytique de la Chaleur*, Chez Firmin Didot Pere et Fils, Paris.
- Frankenstein, G., and R. Garner (1967), Equations for determining the brine volume of sea ice from -0.5° to -22.9°C , *J. Glaciol.*, 6(48), 943–944.
- Freitag, J., and H. Eicken (2003), Meltwater circulation and permeability of Arctic summer sea ice derived from hydrological field experiments, *J. Glaciol.*, 49, 349–358, doi:10.3189/172756503781830601.
- Golden, K. M. (2001), Brine percolation and the transport properties of sea ice, *Ann. Glaciol.*, 33, 28–36, doi:10.3189/172756401781818329.
- Golden, K. M., S. F. Ackley, and V. I. Lytle (1998), The percolation phase transition in sea ice, *Science*, 282, 2238–2241, doi:10.1126/science.282.5397.2238.
- Golden, K. M., H. Eicken, A. L. Heaton, J. Miner, D. J. Pringle, and J. Zhu (2007), Thermal evolution of permeability and microstructure in sea ice, *Geophys. Res. Lett.*, 34, L16501, doi:10.1029/2007GL030447.
- Granskog, M. A., T. Vihma, R. Pirazzini, and B. Cheng (2006), Superimposed ice formation and surface energy fluxes on sea ice during the spring melt-freeze period in the Baltic Sea, *J. Glaciol.*, 52(176), 119–127, doi:10.3189/172756506781828971.
- Grenfell, T. C., and D. K. Perovich (2004), Seasonal and spatial evolution of albedo in a snow-ice-land-ocean environment, *J. Geophys. Res.*, 109, C01001, doi:10.1029/2003JC001866.
- Hanesiak, J. M., D. G. Barber, R. M. Abreu, and J. J. Yackel (2001), Local and regional observations of Arctic first-year sea ice during melt ponding, *J. Geophys. Res.*, 106(C1), 1005–1016, doi:10.1029/1999JC000068.
- Holt, B., and S. A. Digby (1985), Processes and imagery of first-year fast sea ice during the melt season, *J. Geophys. Res.*, 90(C3), 5045–5062, doi:10.1029/JC090iC03p05045.
- Hunke, E. C., and W. H. Lipscomb (2010), CICE: The Los Alamos sea ice model documentation and software user's manual version 4.1, *Rep. LA-CC-06-012*, T-3 Fluid Dyn. Group, Los Alamos Natl. Lab., Los Alamos, N. M.
- Incropera, F. P., and D. P. DeWitt (2007), *Fundamentals of Heat and Mass Transfer*, 6th ed., John Wiley, Hoboken, N. J.
- Kakaç, S., and Y. Yener (1993), *Heat Conduction*, 3rd ed., Taylor and Francis, Washington, D. C.
- Kawamura, T., M. Ishikawa, T. Takatsuka, S. Kojima, and K. Shirasawa (2006), Measurements of permeability in sea ice, paper presented at 18th International Symposium on Ice, Int. Assoc. for Hydro-Environ. Eng. and Res., Sapporo, Japan, 28 Aug. to 1 Sep.
- Kelly, B. P. (1996), Live capture of ringed seals in ice-covered waters, *J. Wildl. Manage.*, 60(3), 678–684, doi:10.2307/3802087.
- Lake, R. A., and E. L. Lewis (1970), Salt rejection by sea ice during growth, *J. Geophys. Res.*, 75(3), 583–597, doi:10.1029/JC075i003p00583.
- Light, B., T. C. Grenfell, and D. K. Perovich (2008), Transmission and absorption of solar radiation by Arctic sea ice during the melt season, *J. Geophys. Res.*, 113, C03023, doi:10.1029/2006JC003977.
- Lüthje, M., D. L. Feltham, P. D. Taylor, and M. G. Worster (2006), Modeling the summertime evolution of sea-ice melt ponds, *J. Geophys. Res.*, 111, C02001, doi:10.1029/2004JC002818.
- Moody, L. F. (1944), Friction factors for pipe flow, *Trans. ASME*, 66(8), 671–684.
- Nazintsev, Y. L. (1964), Teplovoy balans poverkhnosit mnogoletnego lediandogo pokrova v tsentral'noi Arktike, *Aktr. Antarkt. Nauchno-Issled. Inst. Tr.*, 267, 110–126.
- Notz, D., and M. G. Worster (2006), A 1-D enthalpy model of sea ice, *Ann. Glaciol.*, 44, 123–128, doi:10.3189/172756406781811196.
- Ono, N., and T. Kasai (1985), Surface layer salinity of young sea ice, *Ann. Glaciol.*, 6, 298–299.
- Pedersen, C. A., E. Roeckner, M. Lüthje, and J. Winther (2009), A new sea ice albedo scheme including melt ponds for ECHAM5 general circulation model, *J. Geophys. Res.*, 114, D08101, doi:10.1029/2008JD010440.
- Perovich, D. K., and A. J. Gow (1996), A quantitative description of sea ice inclusions, *J. Geophys. Res.*, 101(C8), 18,327–18,343, doi:10.1029/96JC01688.
- Perovich, D. K., T. C. Grenfell, B. Light, and P. V. Hobbs (2002a), Seasonal evolution of the albedo of multiyear Arctic sea ice, *J. Geophys. Res.*, 107(C10), 8044, doi:10.1029/2000JC000438.
- Perovich, D. K., W. B. Tucker III, and K. A. Ligett (2002b), Aerial observations of the evolution of ice surface conditions during summer, *J. Geophys. Res.*, 107(C10), 8048, doi:10.1029/2000JC000449.
- Perovich, D. K., T. C. Grenfell, J. A. Richter-Menge, B. Light, W. B. Tucker III, and H. Eicken (2003), Thin and thinner: Sea ice mass balance measurements during SHEBA, *J. Geophys. Res.*, 108(C3), 8050, doi:10.1029/2001JC001079.
- Petrich, C., P. J. Langhorne, and Z. F. Sun (2006), Modelling the interrelationships between permeability, effective porosity, and total porosity in sea ice, *Cold Reg. Sci. Technol.*, 44, 131–144, doi:10.1016/j.coldregions.2005.10.001.
- Pringle, D. J., J. E. Miner, H. Eicken, and K. M. Golden (2009), Pore space percolation in sea ice single crystals, *J. Geophys. Res.*, 114, C12017, doi:10.1029/2008JC005145.
- Rantz, S. E., et al. (Eds.) (2005), Discharge ratings using simple stage-discharge relations, in *Measurement and Computation of Streamflow*, U.S. Geol. Surv. Water Supply Pap., vol. 2175, chap. 10, pp. 285–388, U.S. Geol. Surv., Reston, Va.
- Scharien, R. K., and J. J. Yackel (2005), Analysis of surface roughness and morphology of first-year sea ice melt ponds: Implications for microwave scattering, *IEEE Trans. Geosci. Remote Sens.*, 43, 2927, doi:10.1109/TGRS.2005.857896.
- Shams, I. H. (1992), *Mechanics of Fluids*, 3rd ed., McGraw-Hill, New York.
- Shapiro, L. H., and P. W. Barnes (1991), Correlation of nearshore ice movement with seabed ice gouges near Barrow, Alaska, *J. Geophys. Res.*, 96 (C9), 16,979–16,989, doi:10.1029/91JC01434.
- Skiplingstad, E. D., C. A. Paulson, and D. K. Perovich (2009), Simulation of melt pond evolution on level ice, *J. Geophys. Res.*, 114, C12019, doi:10.1029/2009JC005363.
- Taylor, P. D., and D. L. Feltham (2004), A model of melt pond evolution on sea ice, *J. Geophys. Res.*, 109, C12007, doi:10.1029/2004JC002361.
- Tschudi, M., J. Maslanik, and D. Perovich (2008), Derivation of melt pond coverage on Arctic sea ice using Modis observations, *Remote Sens. Environ.*, 112, 2605–2614, doi:10.1016/j.rse.2007.12.009.
- White, F. M. (2006), *Viscous Fluid Flow*, 3rd ed., McGraw-Hill, Inc., New York.

Z. Courville and D. Perovich, Terrestrial and Cryospheric Sciences Branch, CRREL, 72 Lyme Rd., Hanover, NH 03755, USA.

C. Polashenski, Thayer School of Engineering, Dartmouth College, HB 8000, Hanover, NH 03755, USA. (chris.polashenski@gmail.com)